



Thermal infrared laser heterodyne spectroradiometry for solar occultation atmospheric CO₂ measurements

Alex Hoffmann, Neil A. Macleod, Marko Huebner, and Damien Weidmann

Space Science and Technology Department (RAL Space), STFC Rutherford Appleton Laboratory, Harwell Campus, Didcot, OX11 0QX, UK

Correspondence to: Damien Weidmann (damien.weidmann@stfc.ac.uk)

Received: 24 April 2016 – Published in Atmos. Meas. Tech. Discuss.: 13 July 2016

Revised: 16 November 2016 – Accepted: 21 November 2016 – Published: 13 December 2016

Abstract. This technology demonstration paper reports on the development, demonstration, performance assessment, and initial data analysis of a benchtop prototype quantum cascade laser heterodyne spectroradiometer, operating within a narrow spectral window of $\sim 1 \text{ cm}^{-1}$ around 953.1 cm^{-1} in transmission mode and coupled to a passive Sun tracker. The instrument has been specifically designed for accurate dry air total column, and potentially vertical profile, measurements of CO₂. Data from over 8 months of operation in 2015 near Didcot, UK, confirm that atmospheric measurements with noise levels down to 4 times the shot noise limit can be achieved with the current instrument. Over the 8-month period, spectra with spectral resolutions of 60 MHz (0.002 cm^{-1}) and 600 MHz (0.02 cm^{-1}) have been acquired with median signal-to-noise ratios of 113 and 257, respectively, and a wavenumber calibration uncertainty of 0.0024 cm^{-1} .

Using the optimal estimation method and RFM as the radiative transfer forward model, prior analysis and theoretical benchmark modelling had been performed with an observation system simulator (OSS) to target an optimized spectral region of interest. The selected narrow spectral window includes both CO₂ and H₂O ro-vibrational transition lines to enable the measurement of dry air CO₂ column from a single spectrum. The OSS and preliminary retrieval results yield roughly 8 degrees of freedom for signal (over the entire state vector) for an arbitrarily chosen a priori state with relatively high uncertainty (~ 4 for CO₂). Preliminary total column mixing ratios obtained are consistent with GOSAT monthly data. At a spectral resolution of 60 MHz with an acquisition time of 90 s, instrumental noise propagation yields an error of

around 1.5 ppm on the dry air total column of CO₂, exclusive of biases and geophysical parameters errors at this stage.

Copyright statement

The works published in this journal are distributed under the Creative Commons Attribution 3.0 License. This license does not affect the Crown copyright work, which is re-usable under the Open Government Licence (OGL). The Creative Commons Attribution 3.0 License and the OGL are interoperable and do not conflict with, reduce, or limit each other.

© Crown copyright 2016

1 Introduction

The accelerating rise of global levels of carbon dioxide in the atmosphere, most likely due to human activity and anthropogenic emissions (Le Quéré et al., 2013), is believed to be the main driver of (anthropogenic) climate change (Myhre et al., 2013). Within the global carbon biogeochemical cycle (Ciais et al., 2013), the regional quantification of terrestrial (and to a lesser extent, oceanic) sources, sinks, and feedbacks remains uncertain, particularly in the tropics (e.g. Le Quéré et al., 2009; Schimel et al., 2015). Likewise, geographical patterns of CO₂ emissions from fossil fuel sources are needed to improve upon the regional land flux estimates (Peylin et al., 2013).

Known as the top-down approach, carbon exchange processes between the atmosphere and the underlying surface are frequently derived from variations in measured near-

surface CO₂ concentrations through inverse techniques based on atmospheric transport models, in order to identify the spatio-temporal distribution of fluxes (e.g. Gurney et al., 2002; Peylin et al., 2013). To achieve this aim, near-surface measurements (continuous or from flask samples; Conway et al., 1994) are commonly used. An increasingly dense and comprehensive observation network and monitoring system operating to high degrees of precision and accuracy is ever more important (Ciais et al., 2010; Marquis and Tans, 2008; Nisbet and Weiss, 2010), as the results of inversions can be very sensitive to the observational network of CO₂ concentrations (Peylin et al., 2013). Requirements on measurement precision and accuracy are extremely demanding. For instance, the WMO/GAW (2014) expert group recommends a target measurement compatibility for the CO₂ in situ mole fraction (i.e. concentration or mixing ratio) in dry air (X_{CO_2}) of 0.1/0.05 ppm in the Northern and Southern hemispheres, respectively, for well-mixed background air. For emission monitoring, an absolute accuracy of 5% or better of the increase with respect to the background is recommended.

The number and frequency of observations can be dramatically increased through remote sensing from space. This has been shown to be potentially very effective in reducing uncertainties related to carbon flux estimations (Boesch et al., 2011; Chevallier et al., 2009), although the assimilation of real data seems as yet not to provide the expected improvements (Chevallier et al., 2014; Houweling et al., 2015). Obviously, the signature of carbon exchange processes is strongest within the atmospheric planetary boundary layer (PBL). In summertime North America, for example, persistent deficits of 4–20 ppm were measured in the lowest 2–3 km of the atmosphere, attributed to a vegetation sink, with smaller deficits in the boundary layer or larger ones in the free troposphere hypothetically related to deep convective overturning (Gerbig et al., 2003). The largest continental variability of up to 20 ppm was found to be confined to the mixed and residual layers, typically limited in altitude between several hundreds of metres and roughly 2 km. Concentrations in the free troposphere were found to have less variability, typically up to ~3 ppm from a marine boundary layer reference. Furthermore, CO₂ increases from nocturnal respiration are likely to be confined to the usually very shallow early morning mixed layers.

Any remote sensing technique hoping to contribute to accurate CO₂ measurements hence needs to be sensitive to the concentration within this lowest atmospheric layer. Also, total column mixing ratios exhibit weaker signatures of surface exchange processes than do actual surface measurements and were found to yield a less precise inversion than classical near-surface sampling (Chevallier et al., 2011). Consequently, requirements on uncertainty may even be tighter than for surface instrumentation.

Already in 2001, Rayner and O'Brien (2001) specified total column monthly averaged measurement precision requirements of 1.5–2.5 ppm for the utility of a (global) mod-

erately sized network to compare with that of existing surface measurements in flux inversions, using simulations. The Total Carbon Column Observing Network (TCCON; Wunch et al., 2011), currently comprising over 20 operational sites equipped with high-resolution Fourier transform spectrometers, provides a basis for present and future satellite observation calibration and validation (e.g. Deng et al., 2014). It sets a new benchmark of 0.2–0.25% (~1 ppm) total error for remotely sensed observations. Deutscher et al. (2010) demonstrated 0.1% relative precision for one of the TCCON sites located in Darwin, Australia. Similar values for total column precision/accuracy over regional scales (around 1 ppm) are also set, targeted, and quoted for spaceborne observations (Boesch et al., 2011; Butz et al., 2011; Ciais et al., 2010; Crisp et al., 2004; Kadyrov et al., 2009; Miller et al., 2007; Thompson et al., 2012), depending on observational frequency, often requiring significant efforts to improve retrievals and spectroscopy.

Besides the potential for global and frequent coverage from space, one possible advantage of column-integrated over surface measurements is that they may reduce uncertainties due to (mostly convective) vertical mixing and transport across the PBL inversion layer and throughout the free troposphere, and hence dilution of the signal (Rayner and O'Brien, 2001; Wunch et al., 2011; Yang et al., 2007), provided such dilution is efficient on the regional scales of interest.

Meanwhile, height-resolved vertical profiles of CO₂, in particular with data points within PBL and in the free troposphere above, constitute a valuable further resource for quantifying advective transport, constraining carbon flux estimates, and verifying inversion results (Crevoisier et al., 2010; Gerbig et al., 2003; Stephens et al., 2007). They can also be used to evaluate the exchange between the PBL and the free troposphere above. Mostly, such data are acquired by profiling using sampling on-board aircraft, although differential absorption and integrated path lidar have also been deployed for both range-resolved and (mostly) path-mean active remote sensing of CO₂ in the PBL and free troposphere (Abshire et al., 2010; Gibert et al., 2008; Koch et al., 2008; Ramanathan et al., 2015).

Whilst TCCON currently provides the best benchmark in ground-based remote sensing of CO₂, the upfront investment in establishing a site and the subsequent running costs are high. In addition, given the size of the FTIR instrument used, the rapid deployment of ad hoc temporary and configurable networks cannot be envisaged. With the objective to provide complementary instrumentation addressing these shortfalls, an alternative approach for generating high spectral resolution spectra of atmospheric transmittance is considered here.

This paper reports on the technical development of a lab- and ground-based thermal infrared (TIR) laser heterodyne spectroradiometer (LHR) aiming at accurately characterizing total column and vertical profiles of CO₂ in solar occultation (solar absorption–atmospheric transmission) mode, building on past instruments successfully used for the passive remote

sounding of a variety of trace gases in the atmosphere (Tsai et al., 2012; Weidmann et al., 2007a, b, 2011a). The prototype instrument has been installed at the Rutherford Appleton Laboratory near Chilton (Didcot), UK, and operated in fair weather conditions since May 2015.

Theoretical principles and a historical perspective on laser heterodyne spectroradiometry are given elsewhere (e.g. Weidmann et al., 2007a, and references therein). In a nutshell, the broadband radiation from the scene, containing the spectral signatures of the gas(es) of interest, is mixed with laser light from a local oscillator (LO). In the simplest implementation, the LO frequency is continuously tuneable and the tuning range determines the spectral coverage of the spectroradiometer. The mixing amplifies the weak radiometric signal and spectrally down-converts it into the radio-frequency (RF) domain, where a high spectral resolution can be set with standard RF filters (the spectral response function of which can be precisely measured), and the signal is recorded with a square-law detector. LHR combines the unique advantages of very high spectral resolution (resolving power $\sim 10^6$) and high sensitivity (ideally shot-noise-limited) with a narrow field of view (FOV). The use of single-mode semiconductor lasers as LO, in this case a quantum cascade laser (QCL), restricts the spectral coverage of the LHR and narrow spectral window optimization is required to specifically target one or a few trace gases (Weidmann et al., 2007a). High spectral resolution, combined with a high signal-to-noise ratio (SNR), is useful to accurately measure an atmospheric line shape, and thus to derive total column trace gas amounts to a high degree of precision or, alternatively, to deconvolve altitudinal (height-resolved) information, both immediately useful in the context of carbon cycle and anthropogenic emission studies. Note here, however, that whilst ultra-high spectral resolution is certainly beneficial for increased accuracy and sensitivity to Doppler-limited line widths in low pressure upper atmospheres (e.g. Kostiuk et al., 1977), from a retrieval perspective, such high resolution may not be similarly advantageous to sounding in the high pressure PBL, particularly if this needs to be achieved at the expense of SNR. As a rule of thumb, heterodyne detection trumps over direct detection at long wavelengths and very high spectral resolution. Compared with other remote sensing techniques, LHR also has a high potential for miniaturization and ruggedization, e.g. through hollow waveguide integration (Weidmann et al., 2011b), which makes it well suited for field, air-, and spaceborne deployment, individually or in a networked configuration.

Mid-infrared laser heterodyne detection is almost as old as the laser (Teich et al., 1966); see applications and reviews by e.g. Kostiuk and Mumma (1983) and Parvite et al. (2004). For example, earlier work on LHR with tuneable diode lasers relied on larger and less capable LOs, such as lead salt lasers (Frerking and Muehlner, 1977). The heterodyne technique, using diode or (CO_2) gas lasers and only much later using QCLs, had successfully been applied to ground-based stud-

ies of the Earth's atmosphere (e.g. Abbas et al., 1979; Fast et al., 2004; Glenar et al., 1982; Koide et al., 1995; Menzies and Seals, 1977) and that of other solar system bodies (Kostiuk et al., 1977, 2001; e.g. Kostiuk, 1994; Sonnabend et al., 2006), in terms of composition, structure, and dynamics, as well as in other areas of astronomy. However, technical limitations in the quality of solid-state LOs in early work had impeded a rapid expansion of the technique (Parvite et al., 2004). The instrument presented here, beyond applying the technique to the sounding of highly relevant CO_2 , also leverages the increased stability, high optical power, frequency tuning, single-mode emission, and spectral purity of distributed feedback QCLs, also utilized by other groups (e.g. Sonnabend et al., 2008; Wirtz et al., 2002). Their compactness and operability at room temperature are highly desirable for full optical integration and operation in extreme environments. This work also systematically characterizes the performance of the instrument over an extended measurement period, a prerequisite for a successful application to long-term greenhouse gas monitoring, and documents an initial assessment of what information can be expected from data retrieval.

The use of LHR for CO_2 monitoring is also currently being investigated by Clarke et al. (2014), Melroy et al. (2015), and Wilson et al. (2014). Their system operates in the short-wave IR ($1.6 \mu\text{m}$), leveraging telecommunication distributed feedback lasers as the LO and associated photonics components to couple the solar radiation to a single-mode optical fibre connected to the solar trackers of the AERONET Sun photometer network. Conversely, we use QCLs to operate in the thermal infrared. Not only is a TIR LHR of interest to look into the measurement consistency across spectral bands, but the ideal SNR of laser heterodyne systems also scales with the wavelength. For instance, considering a radiation emitted from the Sun equivalent blackbody, the ideal LHR SNR is improved by ~ 15 times at 960 cm^{-1} compared to 6500 cm^{-1} . In addition, access to the fundamental intense ro-vibrational bands in the TIR is more suited for probing trace atmospheric species, and atmospheric scattering is smaller.

2 Prior analysis and benchmark performance modelling

2.1 Generic description of the approach

Distributed feedback semiconductor lasers exhibit narrow spectral windows of continuous frequency tuning. The central frequency of these narrow windows can be precisely tailored, either by material composition change for laser diodes or band engineering for QCLs. As far as atmospheric sounding is concerned, these features ought to be considered as part of prior analysis to define and select the optimized narrow spectral windows well suited for, in this particular case, CO_2 remote sensing. This prior analysis may help the instrument design by (a) maximizing the information content obtained

by the measurements, (b) considering the addition of alternate atmospheric constituents such as H₂O to be measured simultaneously and hence allowing calculation of dry air CO₂ mixing ratios, and (c) minimizing spectral interferences from other narrow band absorbers to limit the possibility of model errors. The general approach to prior analysis consists of building an observing system simulator (OSS) consisting of (1) a forward model describing the remote sensing scenario and radiative transfer (instrument and atmosphere), (2) an optimum estimation retrieval algorithm, and (3) a set of analysis tools to quantify sounding performances.

The forward modelling component of the OSS built to analyse LHR performances includes the MIPAS Reference Forward Model, RFM (Dudhia, 1997, 2017), version 4.33. The program is iteratively called to calculate atmospheric radiative transfer and the associated Jacobian matrix (\mathbf{K}). RFM is set to use 100 internal layers (every 0.5 km up to 10 km, then every 1 km up to 90 km). Jacobians are calculated with applied perturbations centred on a retrieval level and linearly tapered off up to the adjacent retrieval levels. The HITRAN 2012 (Rothman et al., 2013) spectral database provides the molecular absorption line parameters; Voigt line shapes are used by RFM as default. For simulation purposes, pressure, temperature, and potentially interfering species (O₃, N₂O, NH₃, COF₂) profiles have been set equal to the typical mid-latitude MIPAS 2001 reference atmosphere compiled for the MIPAS instrument on board the ENVISAT satellite (Dudhia, 1997). Realistic, “true” reference H₂O and CO₂ profiles are inserted that have been constructed to exhibit larger structural variability than the standard profiles. A water vapour profile measured on 31 July 2015 by operational radiosonde has been converted from mass to volume mixing ratio before insertion. An artificial CO₂ profile has been generated with a depression in the PBL, hypothetically accounting for plant uptake of CO₂, and with random variability on a slowly varying background throughout the full atmospheric column, which is roughly aligned with in situ aircraft measurements used as reference by Ramanathan et al. (2015).

The forward model also includes an LHR instrument model (Weidmann et al., 2007a), primarily to work out the SNR delivered by the instrument as function of instrumental parameters such as integration time, spectral resolution, and sampling resolution. With adequate detectors, laser heterodyne radiometry is ideally LO shot-noise-limited (Weidmann et al., 2007a). In practice, real noise levels are expected to be above the shot noise limit. It is therefore realistic to simulate instrument performance at the shot noise limit to provide the ultimate benchmark reference against which experimental data are to be compared. In the OSS, LO shot noise is mapped into the transmission domain, assuming the radiating background is an ideal blackbody at 5778 K (see Sect. 4.3). In other words, no account of potential broadband atmospheric absorption is factored in, hence simulating the

upper limit in terms of performance. Random noise is added to the synthetic spectra assuming a normal distribution.

The second component of the OSS is the optimal estimation algorithm (OEA). Its role consists in providing the best estimate possible of the quantities being measured given our knowledge of the atmospheric state and information provided by the LHR recorded spectra. CO₂ profiles and total column amounts are ultimately determined by an inverse modelling-based retrieval. Height information in vertically resolved profiles comes from the temperature and pressure dependence of the absorption line shapes; atmospheric temperature and pressure profiles are assumed to be known from auxiliary data sources. The OEA involves the non-linear least squares fitting of a forward-modelled spectrum ($F(\mathbf{x})$), integrating the trace gas concentrations to be estimated (i.e. the state vector \mathbf{x}), to a measured spectrum (\mathbf{y}) with measurement error ($\boldsymbol{\epsilon}$), expressed as an error covariance matrix $\mathbf{S}_{\boldsymbol{\epsilon}}$, and starting from a prior state (\mathbf{x}_a) with an a priori covariance matrix \mathbf{S}_a . The details of the OEA are beyond the scope of this paper. Suffice to say that the retrieval is built around a well-established methodology (Rodgers, 2000), using Bayesian statistics with Gaussian probability density functions and a Levenberg–Marquardt iterative procedure to minimize the cost function (χ^2):

$$\chi^2 = [\mathbf{y} - \mathbf{F}(\mathbf{x}_i)]^T \mathbf{S}_{\boldsymbol{\epsilon}}^{-1} [\mathbf{y} - \mathbf{F}(\mathbf{x}_i)] + [\mathbf{x}_i - \mathbf{x}_a]^T \mathbf{S}_a^{-1} [\mathbf{x}_i - \mathbf{x}_a]. \quad (1)$$

Trace gases are typically (but not necessarily) solved for as the natural logarithm of their volume mixing ratio to constrain the algorithm to positive concentrations and improve the handling of large dynamic ranges. The retrieval code can be run with the purely synthetic data provided by the forward model (pseudo-observations), thus completing the OSS to study the anticipated instrument performance.

In addition, the OEA offers quantitative tools to analyse the observing system performance and identify an optimal spectral region; the most useful of these are the Shannon information content (H) and the degrees of freedom for the signal (d_s) (Rodgers, 2000):

$$H = -0.5 \cdot \ln |\mathbf{I}_n - \mathbf{A}|, \quad (2)$$

$$d_s = \text{tr}(\mathbf{A}), \quad (3)$$

where \mathbf{I}_n is the unit matrix of order n (the number of state vector elements). The averaging kernel matrix $A_{ij} = \partial \hat{x}_i / \partial x_j$, giving the sensitivity of the retrieved state ($\hat{\mathbf{x}}$) to the true state (\mathbf{x}), is calculated as

$$\mathbf{A} = \left(\mathbf{K}^T \mathbf{S}_{\boldsymbol{\epsilon}}^{-1} \mathbf{K} + \mathbf{S}_a^{-1} \right)^{-1} \mathbf{K}^T \mathbf{S}_{\boldsymbol{\epsilon}}^{-1} \mathbf{K}. \quad (4)$$

The combination of forward modelling, OEA, and the corresponding information content analysis tools completes the OSS and is then used in the practical case of CO₂ sounding using a LHR operating from the ground in solar occultation.

2.2 Implementation for CO₂ sounding

In a preliminary survey of spectral regions aimed at assessing thermal infrared LHR performance for trace gas sounding, Rose and Weidmann (2013) identified the ($\nu_1 \leftarrow \nu_3$) hot absorption band centred around 960 cm^{-1} as suitable for solar occultation measurements, unlike the much stronger ν_2 fundamental band, centred at 662 cm^{-1} , which was better suited for nadir and limb emission soundings. At 960 cm^{-1} , the spectrum of CO₂ consists of a well-defined P–R band structure of absorption lines typically spaced by $\sim 2\text{ cm}^{-1}$. In a first instance, the OSS was used iteratively in conjunction with a “sliding” narrow spectral window. Figure 1 shows the evolution of the information content for both CO₂ and H₂O retrieval as a window of 1 cm^{-1} is slid by 0.2 cm^{-1} steps. CO₂ information content follows the ro-vibrational band structure. Focusing on the P branch, in which QCLs were more readily available at the time of the instrument development, the window centred at 953.1 cm^{-1} was found to be a good compromise for optimum remote sounding of both CO₂ (22 bits) and H₂O (20 bits). Additionally, in this window, any other potential narrow-band atmospheric absorber contributes to less than 10^{-3} in absorption based on a typical mid-latitude atmosphere. The CO₂ line retained for this work is the P10 transition around $952.880849\text{ cm}^{-1}$ ($10.5\text{ }\mu\text{m}$) with an intensity of $1.9 \times 10^{-23}\text{ cm}^{-1}/(\text{molec cm}^{-2})$. The H₂O line within the narrow window is centred at $953.367430\text{ cm}^{-1}$, has an intensity of $4.801 \times 10^{-24}\text{ cm}^{-1}/(\text{molec cm}^{-2})$, and belongs to the ν_2 fundamental band.

The corresponding averaging kernels (AKs) were calculated for illustration purposes using a dense vertical retrieval grid with 0.5 km spacing and are shown in Fig. 1b and c. The AKs can be interpreted as the vertical sensitivity of the measurement and show that the measurement should be most sensitive to the lowest tropospheric layers, in particular to CO₂ and H₂O concentrations within the PBL. Using the metric of the sum of the AKs < 0.8 , the CO₂ sensitivity goes up to 25 km and then tails off at -0.05 km^{-1} , while the water sensitivity reaches 8 km and then drops at a rate of -0.5 km^{-1} . Since CO₂ is assumed to be a reasonably well-mixed gas (with the profile used for simulating the spectrum reflecting this), the averaging kernels decay with the atmospheric exponential pressure decrease with height, determining the absolute number of absorbing molecules within a given layer. Likewise, the averaging kernels for H₂O decay with the typical altitudinal distribution of water vapour, for which freeze-drying results in only trace amounts above the tropopause.

Once the optimum LHR narrow window has been chosen, a more targeted analysis can establish the ideal benchmark against which measurements are to be compared. The simulation represents a best-case scenario of a shot-noise-limited instrument without biases (systematic errors) or other error sources in the observing and retrieval system.

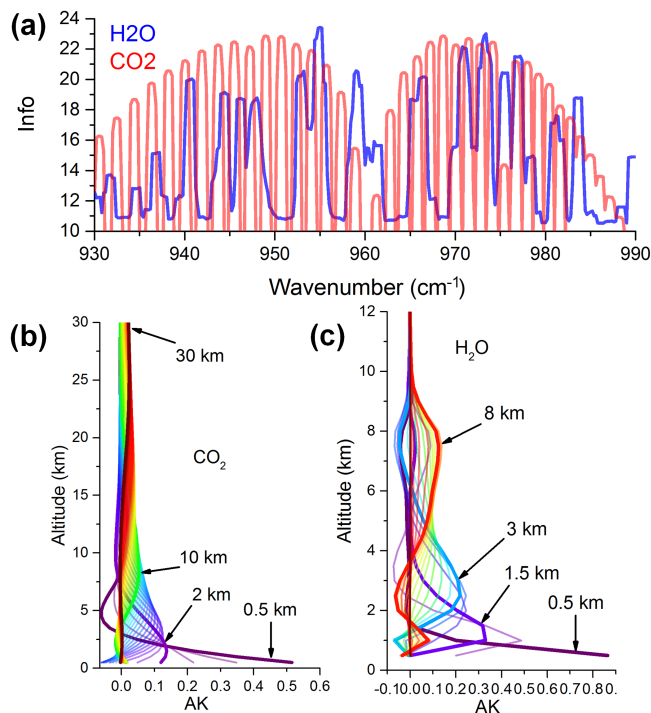


Figure 1. (a) Observing System Simulator retrieved Shannon information content for CO₂ and H₂O for a narrow spectral window of 1 cm^{-1} , successively slid by 0.2 cm^{-1} over the full spectral range; (b) CO₂ and (c) H₂O high-resolution averaging kernels computed for the finally selected narrow spectral window. The four thick lines pointed at by arrows correspond to the state vector heights used in the instrument performance simulation (Fig. 2).

Within the OSS, the state vector \mathbf{x} concatenates the altitudinal profile of both CO₂ and H₂O to be retrieved, as well as one coefficient (a_0) that describes the linear mapping (radiance scaling) from atmospheric transmission to heterodyne signal and potential broadband absorption not included in the forward model. This coefficient is initially set to 1. The a priori \mathbf{x}_a is taken from the MIPAS reference atmosphere, standard errors on \mathbf{x}_a are arbitrarily set to 20, 50, and 100 % for CO₂, H₂O, and a_0 , respectively, and \mathbf{S}_a is also assumed diagonal. These assumptions do not necessarily reflect the optimum conditioning of the retrieval; in the context of this work the objective is to benchmark the first outcomes from the instrumental development of the TIR LHR and focus on instrument error. The altitudes on which to retrieve CO₂ and H₂O have been chosen by iteration such that (i) the size of the state vector n is close to d_s , (ii) the averaging kernels cover the entire retrievable column with approximate overlap at their half-maxima (see Fig. 1b and c), (iii) the retrieved layers give enough vertical resolution to capture highest variability within the PBL, (iv) retrieval sensitivity to the exact state vector configuration is limited, and (v) the residuals after the fit exhibit no obvious bias. The solar elevation angle was set to 60° . The simulated instrument integration time

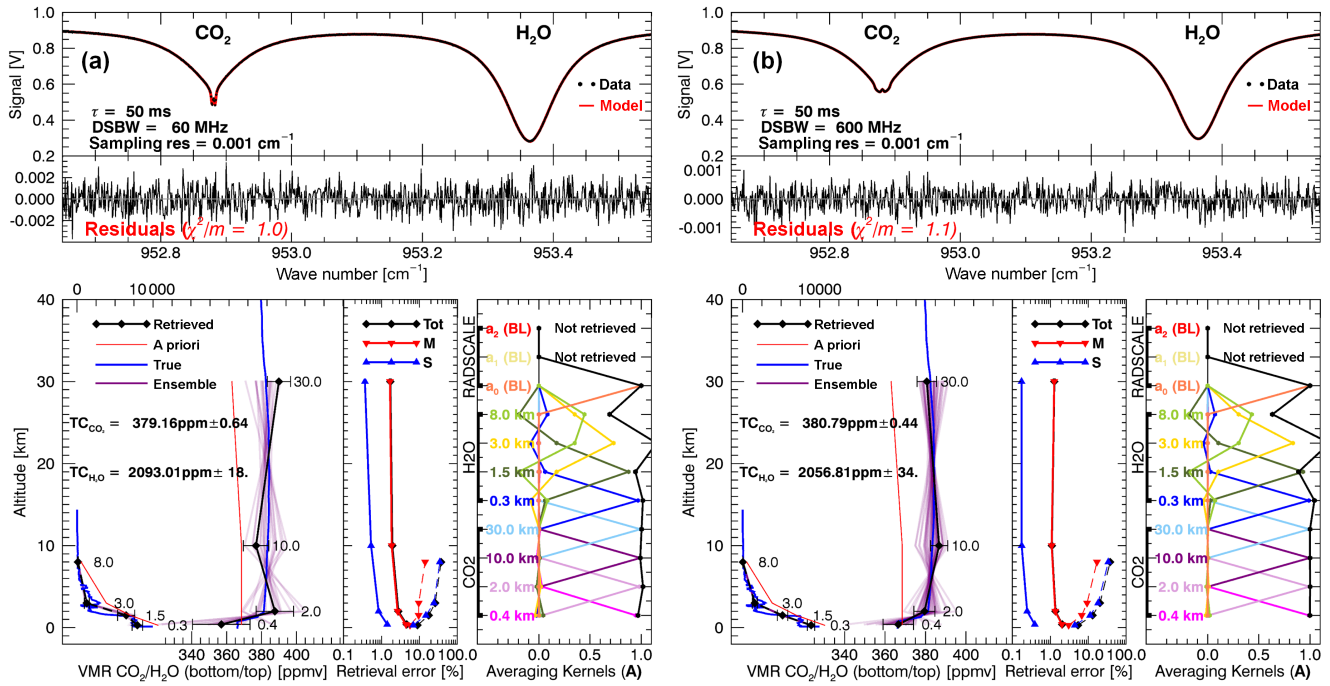


Figure 2. OSS simulation for the selected spectral narrow window under the assumption of a shot-noise-limited operation of the LHR with a 60° Sun elevation. Instrument spectral resolutions (double side bandwidth, DSBW) are set to (a) 60 MHz and (b) 600 MHz. The top panel shows a synthetic spectrum (data) with noise, calculated from a known “true” state of the atmosphere. Superimposed is the retrieved spectrum (model), and the difference is shown as residuals below. The bottom panel depicts all (purple) and one selected (black) amongst the retrieved state ensemble members as separate H₂O and CO₂ profiles, in comparison to the true and a priori state (left). Error bars characterize the retrieval uncertainty at the state vector altitudes. The estimated total columns (TC) with uncertainties are given as text. Total retrieval errors (Tot) and contributions from measurement noise (M) and smoothing error (S) are shown as profiles in the centre. The averaging kernels for the composite state vector are shown on the right; RADSCALE denotes the instrument baseline (BL), which corresponds to a 1 : 1 mapping from radiometric into signal voltage for these simulations.

was 50 ms, and ideal shot-noise-limited operation was assumed. The same instrument line shape (ILS) as measured for the real instrument, and similar values for the sampling resolution (0.001 cm^{-1}) have been introduced.

Using the OSS, an ensemble of 50 retrievals at 600 MHz (20 at 60 MHz) is run, each member differing only by the random seed used to generate the Gaussian measurement noise, used in turn to degrade the synthetic spectrum, and inserted (squared) onto the diagonal elements of \mathbf{S}_e . Results are shown in Fig. 2a and b in which the LHR spectral resolution was set to 60 MHz (0.002 cm^{-1}) and 600 MHz (0.02 cm^{-1}) respectively. The upper part of the figures shows the actual LHR spectra overlaid with the fitted ones. Residuals from the fits are shown below. The lower panels show the retrieval outcomes. For each spectral resolution, the following data are shown from left to right: the H₂O profile, the CO₂ profile, the CO₂ and H₂O retrieval errors, and the averaging kernels. In the profile plots are shown: the a priori profile (red line), the “true” profile used in the OSS, the successive 50 retrieved ensemble member profiles (in transparent purple), and the first member profile from the set (black with error bars). Both the retrieved water and CO₂ profiles (and in particular their

ensemble average, not shown) converge very close to the “truth” used in the OSS. The variability of the 50 retrievals in the CO₂ case exhibits some unphysical oscillations, yet still within the 1σ error bars. Both measurement (M in the figure, from $\mathbf{S}_M = \mathbf{G}\mathbf{S}_e\mathbf{G}^T$, where $\mathbf{G} = \partial\hat{\mathbf{x}}/\partial\mathbf{y}$ is the gain matrix) and smoothing (S, from $\mathbf{S}_S = (\mathbf{I}_n - \mathbf{A})\mathbf{S}_a(\mathbf{I}_n - \mathbf{A})^T$) retrieval errors are shown. In the case of CO₂, retrieval error is dominated by measurement error, which implies that smoothing and the influence of the a priori on the retrieved state are almost negligible. This is anticipated, since \mathbf{x}_a was specified with large uncertainties and without off-diagonal correlation terms on \mathbf{S}_a . Conversely, the H₂O error is dominated by smoothing error. This is particularly the case at higher altitudes, where the system is no longer very sensitive to the actual water vapour concentrations and a priori knowledge therefore significantly contributes to the solution. Note, though, that all the ensemble members are essentially collocated and that a (bias-free) LHR system seems to be very accurate in reconstituting the true, yet smoothed, H₂O profile.

From the retrieval profiles, column measurements can be obtained and are shown in Table 1. Loosely following e.g.

Table 1. Summary of column measurements and errors from the OSS. Values under the error propagation header correspond to the first ensemble member. The planetary boundary layer (PBL) column is here defined as between 0 and 1.2 km.

Quantity	Truth	60 MHz spectral resolution		600 MHz spectral resolution	
		Error prop. ^c	Statistical ($\mu \pm \sigma$) ^d	Error prop.	Statistical ($\mu \pm \sigma$)
Info content ^a H [bit]		50.2		61.7	
DFS ^a d_s (–) (CO ₂ /H ₂ O) ^b		7.9 (3.9/3.0)		8.2 (4.0/3.2)	
CO ₂ column (ppm)	380.52	379.16 ± 0.64	380.19 ± 0.81	380.79 ± 0.44	380.31 ± 0.50
H ₂ O column (ppm)	1920	2093 ± 19	2099 ± 9	2057 ± 35	2056.3 ± 1.5
X _{CO₂} (ppm)	380.69	379.36 ± 1.29		380.98 ± 1.21	
CO ₂ PBL column (ppm)	367.91	356.94 ± 16.48	357.26 ± 17.78	366.58 ± 7.53	366.13 ± 7.95

^a Shannon information content (H) and degrees of freedom for signal (d_s) follow the terminology and notation in Rodgers (2000) and are defined in Eqs. (2) and (3). ^b Values under parentheses correspond to partial DFS for CO₂ and H₂O, respectively, averaged over all ensemble members. ^c Error propagation columns hold retrieved quantities, retrieval errors, and other retrieval diagnostics following the optimal estimation inverse method.

^d Statistical columns hold mean (μ) and standard deviation (σ) calculated over the simulation ensemble members.

Boesch et al. (2011) and O’Dell et al. (2012), the estimates of total vertical column amounts VC and associated variances σ_{VC} have been calculated, respectively, as

$$VC_g = \mathbf{h}_g^T \hat{\mathbf{x}}_g, \quad (5)$$

$$\sigma_{VC_g}^2 = \mathbf{h}_g^T \hat{\mathbf{S}}_g \mathbf{h}_g, \quad (6)$$

where the subscript g indicates the vector section or block matrix corresponding to trace gas g (either CO₂ or H₂O) of the retrieved state and error covariance matrix (identified by hat), $\hat{\mathbf{S}} = (\mathbf{K}^T \mathbf{S}_e^{-1} \mathbf{K} + \mathbf{S}_a^{-1})^{-1}$. To calculate the pressure weighting function h_g the following steps are taken: (i) the air’s molecular number density profile is calculated from the ideal gas law using input temperature and pressure profiles interpolated onto a fine vertical grid up to the top of the atmosphere, (ii) for each retrieval grid level i , the associated $h_{g,i}$ element is computed as the vertically integrated molecular number density between the mid-points (or ground level) centred on altitude i , and (iii) the number of molecules of trace gas g follows trivially through multiplication by the retrieved volume mixing ratio (VMR). The (moist air) total column-averaged VMR and error (TC and σ_{TC} , Table 1) follow by dividing VC (σ_{VC}) by the air’s total column-integrated molecular number density.

An alternate error estimation has been carried out using the ensemble of 50 (20) retrievals from identical synthetic observations and calculating the standard deviation over the TCs estimated for the individual ensemble members. X_{CO_2} is the column-averaged CO₂ mole fraction in dry air following the calculation in Deutscher et al. (2010); its error has been estimated for illustrative purposes using the variance formula error propagation simplification with a surface pressure (p_{srf}) uncertainty arbitrarily set to 3 hPa.

From Table 1, it appears that the errors calculated using error propagation (i.e. from $\hat{\mathbf{S}}$) and the standard deviation calculated over the ensemble (for total column amounts as for individual retrieval levels, not shown except in PBL) are consistent for CO₂, which gives confidence in the retrieval’s

robustness. Individually retrieved total column amounts are within < 1 ppm of their true value and precision is down to < 1 ppm. Individual profiles do not coincide with the true profile, and they exhibit some of the oscillatory characteristic of under-constrained retrievals, but their ensemble average approaches the true profile. For H₂O, the retrieval error exceeds the standard deviation over the ensemble, which is likely due to smoothing. These results imply that LHR can potentially comply with the high-accuracy requirements of CO₂ observing systems aimed at flux inversions and can potentially discriminate the PBL from the free troposphere above, albeit with a relatively high uncertainty under the SNR condition of the OSS runs. The degrees of freedom for signal (over the entire state vector) imply that eight (or possibly more) independent pieces of information can be retrieved from a spectrum (~ 4 for CO₂ profile and > 4.5 on an optimized dense retrieval grid; not shown). Additional systematic errors and biases in real observations as opposed to simulations, not considered in this work, may be highly detrimental to the measurements, and require identification and elimination or accounting for. This is particularly true for spectroscopic and line shape parameters; for example, the CO₂ line intensity used here has been specified with an error larger than 20 % in HITRAN 2012 (all other CO₂ line parameters are specified within the lowest uncertainty classes, whilst uncertainties are larger for H₂O). This possibly warrants acquiring new spectroscopic parameters, a task that is not intractable since the LHR spectra presented herein rely on only two separate lines.

The next sections investigate to what extent the performance of a real system matches the predicted (shot-noise-limited) one. Performances can be improved by using longer integration time. The conditions presented in the OSS correspond to only 90 s per measurement.

3 Instrument design, assembly, and specification

3.1 Laser heterodyne receiver

The breadboard prototype CO₂ LHR assembled for this work follows the overall system design of previous iterations of the instrument (Weidmann et al., 2011a) with significant upgrades in terms of solar tracking and a parallel mixing arrangement rather than convergent. The optical layout of the system is shown in Fig. 3a. The QCL operates single mode with an operating wavelength of $\sim 10.47 \mu\text{m}$ (955 cm^{-1}) and a tuning range of $\sim 7 \text{ cm}^{-1}$ via temperature and current modulation, hereafter simply referred to as tuning (Alpes Lasers SA). It operates in continuous mode at ambient temperatures ($< 40^\circ\text{C}$) with up to 30 mW of power, which is more than sufficient for heterodyne detection. The object beam waist in the QCL facet plane was measured to be $8 \mu\text{m}$. The diverging QCL beam is collimated by a molded aspheric lens (component CL in Fig. 3a; 4 mm effective focal length, 0.56 numerical aperture) and passed through a wire-grid polarizer used as an adjustable attenuator (ATT) to allow the optimum LO power to be selected. A beam expander follows, consisting of two off-axis parabolic mirrors (OAPM1 and OAPM2) in an anti-symmetrical arrangement to reduce potential aberrations. Upon reflection by the beam splitter (BS, wedged ZnSe, 25% reflection), the beam is focused onto the cryogenically cooled high-speed photodiode (PD1, 1 GHz bandwidth HgCdTe photomixer, Raytheon) by OAPM3. Beam expansion is necessary to match the (image) beam waist to the detector element size ($100 \mu\text{m}$ diameter). The requirement is to illuminate 80% of the photodiode active area with 99% of the LO beam encircled energy. Assuming a typical M^2 parameter of a QCL of 1.2, this yields a targeted beam waist of $\sim 30 \mu\text{m}$ in the detector plane and thus an overall magnification requirement of about three. The overall magnification of the LO optical arm is 3.18.

The 75% of LO radiation transmitted by the BS is directed through a $76.10 \pm 0.01 \text{ mm}$ long Germanium etalon for real-time relative laser frequency calibration during the QCL tuning. OAPM4 is used to focus the beam onto a slow TE-cooled photodiode (PD2, Vigo Systems PVM-4TE-10.6).

Additional optics channel the solar longwave radiation, collected by a solar tracker after transmission through the atmosphere, onto the BS where it is spatially superimposed with the LO beam. The solar radiation goes through a longwave-pass filter (LWP), transmitting radiation above $\sim 7.7 \mu\text{m}$ (90% transmission at $10.5 \mu\text{m}$). The optical power reflected by the filter is directed onto a wide-area near-infrared (NIR) broadband Germanium photodiode (NIR PD, New Focus model 2033, 3 dB spectral response from 1100 to 1600 nm) as a solar intensity diagnostic, alignment aid, and cloud monitor. The transmitted longwave radiation passes through an afocal system (OAPM4 and OAPM5) producing a Sun image at which a mechanical chopper is positioned

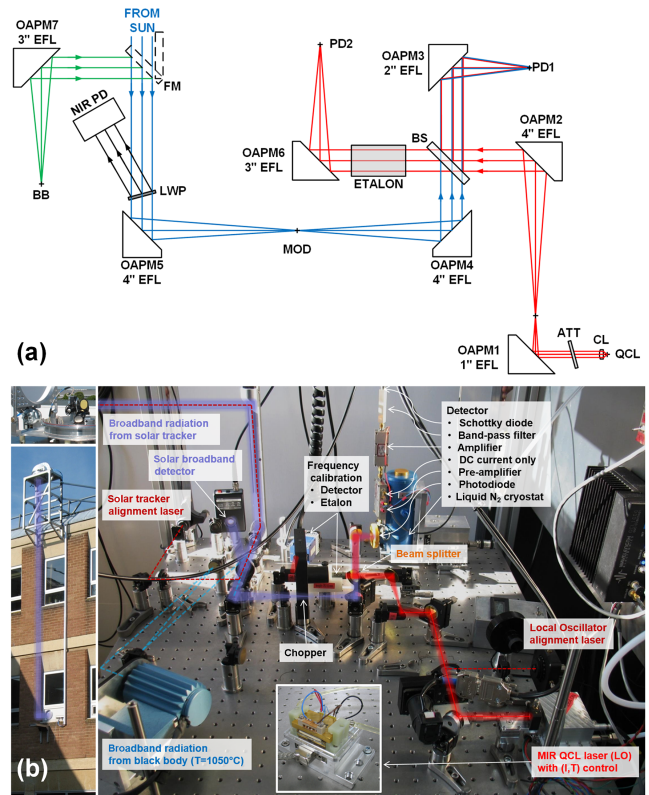


Figure 3. (a) Schematic of the LHR optical layout with the optical path of the LO in red and Sun broadband radiation in blue; (b) annotated picture of the breadboard prototype, next to the outdoor wall-mounted structure with optical path used for solar tracking.

(MOD, model TTI C-995, operating at 1777 Hz) to provide signal amplitude referencing.

In order to estimate the heterodyne field of view and the aperture contributing to the heterodyne signal at the (lock-in) modulation plane (MOD), Gaussian beam back propagation of the LO image formed on PD1 is considered. At the MOD, the optical system provides a 6.4 magnification relative to the beam waist at the QCL facet plane. The back-propagated LO far-field full beam divergence after the final optic (OAPM5) is $\sim 0.83 \text{ mrad}$ and represents the coherent FOV of the instrument. This corresponds to about 1/11 of the apparent solar disc angle.

No radiometric calibration is needed for the LHR operating in transmission mode. However, a calibrated source (a compact blackbody held at 1050°C) can be branched into the instrument's FOV via a flip mirror to quantitatively characterize the radiometric performance of the system.

The output of PD1 is fed in to an AC/DC splitter and an amplifier chain. The DC output is used to monitor the LO power which changes (is modulated) with the frequency tuning. The AC component (heterodyne) is filtered through an RF bandpass filter, which defines the LHR spectral resolution and instrument line shape (see Fig. 1 in Weidmann et al.,

2007b) for a characteristic measured ILS as set by the spectral response of an RF filter). Filters with bandpass ranges of either 50–80 MHz or 50–350 MHz have been used to set the double side band spectral resolution to 60 and 600 MHz respectively. Note here that double side bandwidth (in the frequency domain) and spectral resolution are used interchangeably in spite of the relatively large hole (100 MHz) in the centre of the ILS and thus a correspondingly larger section of the spectrum being affected by the convolution; this is under the assumption that spectral resolution is defined as the mean of the ILS function. The RF power is then detected by a Schottky diode (Eclipse Microwave EZR0120A3) whose output is fed into a lock-in amplifier (Ametek Signal Recovery 7265 DSP) synchronized with the chopper located at the MOD. The lock-in integration time τ has been set to 50 ms for the majority of measurements. Under these conditions the total acquisition time per spectrum is 90 s.

Purpose-built LabVIEW software controls the signal acquisition process. A DAQ-card (NI USB-6259) acquires the in-phase and out-of-phase heterodyne signals from the lock-in amplifier, the DC signals from PD1, the calibration and reference signals from PD2 and NIR PD, and a collection of metadata, including operating parameters.

The QCL is controlled in temperature and current using low noise linear controllers. It has been housed in a custom-built high stability mount. Indeed, the sensitivity of the coherent mixing onto PD1 is critical and highly sensitive to the QCL facet position. Changes in laser temperature are used for coarse wavelength tuning, whilst a current ramp produces laser frequency sweeps over a $\sim 1 \text{ cm}^{-1}$ span. To target the selected narrow spectral window identified, the QCL operates at $477 \pm 85 \text{ mA}$ and $\sim 9.0^\circ\text{C}$.

3.2 Passive solar tracker

Previous LHR atmospheric measurement campaigns (Weidmann et al., 2007a, 2011a) were carried out using an active solar tracker using quadrant detectors and a feedback loop to maintain alignment with the Sun. This system was found to be extremely sensitive to cloud coverage and systematically ceased normal operation upon the slightest reduction in collected solar brightness. This is not viable for the prospect of an unattended autonomous ground-based LHR operating in mid-latitudes. A benefit of TIR transmission LHR is the provision of a large number of observations by leveraging the relatively fast measurement time and extremely narrow FOV, advantageous in a scattered cloud field (compared to say, a pure emission sounder requiring a much larger FOV and/or acquisition time to achieve a comparable SNR). In other words, to be able to pick up good quality data “between clouds”, the system ought to be resilient to clouds passing by the FOV.

To enable this, a passive altazimuth tracking system has been developed that relies on a Sun trajectory algorithm. Our assembly consists of two protected gold-plated

$50.8 \times 25.4 \text{ mm}^2$ elliptically shaped flat mirrors on motorized rotation stages. The azimuth stage has a 50 mm diameter central aperture, through which the radiation is projected vertically downwards onto a folding mirror, passing through a BaF₂ window at the base of the assembly. The solar tracker is mounted in a remote- and environment-controlled protective dome on the roof of a building with almost unobstructed hemispherical viewing capability. The LHR has been assembled on a portable workstation placed directly in front of the window port through which the solar radiation enters (Fig. 3b).

Since the LHR’s FOV only covers a fraction of the apparent Sun disc, and assuming isotropic radiance as a first approximation, pointing accuracy and precision requirements are not stringent as far as the stability of solar power received is concerned. However, very accurate and precise pointing knowledge is required in order to avoid significant bias at the data retrieval stage. Indeed, column retrieved data are highly sensitive to the effective air mass sounded, particularly at low elevation angles. Gisi et al. (2011), for example, specify a 19 arcsec tracking precision requirement to achieve 0.1 % trace gas total column precision at 10° elevation. Our motion system is built around two high-performance rotation stages (Thorlabs NR360S NanoRotators, controlled by a BSC102 APT stepper motor controller). These are specified to provide a maximum accuracy over a 10° range of 5 arcmin ($\sim 0.08^\circ$) and a minimum incremental motion of < 1 arcsec ($\sim 0.0002^\circ$). Mirror alignment, levelling, tracker systems testing, and pointing assessment have been performed using medium-distance (several metres) visible laser circuits and surveying equipment. Horizontally level pointing during azimuth rotation over a range of 180° was achieved to within an error of $\sim 0.2^\circ$. Repeated azimuth and elevation pointing precision from any angular position was measured to be < 1.8 arcmin (0.03°) without intermittent homing; it was found that homing was detrimental to the precision.

A first iteration of the Sun trajectory algorithm embedded within the tracker’s LabVIEW control software is the SUNAE algorithm by Michalsky, Harrison, and Wiscombe, based on a revision of Michalsky (1988) without the atmospheric refraction correction. This specifies an accuracy of better than 0.1° for elevations above 9° , which can be improved to 0.01° with refraction correction, and was deemed one of the most accurate algorithms amongst those reviewed by Blanco-Muriel et al. (2001). This algorithm can be swapped with more accurate and complex ones if necessary (Blanc and Wald, 2012; e.g. Grena, 2012; Reda and Andreas, 2004), but this is unlikely to much improve the system if it is limited by the mechanical and alignment accuracy.

Solar tracking is performed in iterated discrete steps, typically 5–10 s apart. For an altazimuth mount, the apparent azimuth and elevation angular velocities are non-linear functions of date, time, and latitude, which we have calculated as numerical derivatives. For our location, the azimuth angular velocity is larger than that for elevation and reaches

a maximum at local noon around the summer solstice of $0.0081^\circ \text{ s}^{-1}$. With a 10 s update period, this corresponds to a 5 arcmin angular deviation or a trace over 16 % of the Sun disc. Practically, this value is an upper limit and will usually be smaller. In the case of elevation, following the same reasoning, the worst-case scenario pointing accuracy is 1.6 arcmin, which propagates to a < 1 % relative accuracy on the column measurement for elevation $> 3^\circ$, assuming the air mass is inversely proportional to the sine of the elevation angle.

Experimentally, over the course of almost 1 year of operation, it was found that unsupervised tracking can satisfactorily be performed over several hours and up to a day without needing to recalibrate the tracker with no noticeable impact on the measured signal. For comparison, the AERONET four-quadrant active solar tracker used by Wilson et al. (2014) has a stated accuracy of better than 0.1° . However, given the stringent accuracy requirements on X_{CO_2} translating into tolerances on air mass uncertainties, better pointing accuracy and knowledge will eventually be required, especially at low elevation. This, in turn, will be achieved with a complementary active feedback mechanism using a Sun disc imaging camera, in a future iteration of the instrument. Pointing tolerances will need further evaluation using the full retrieval suite for error quantification and proper accounting of measurement biases.

4 Instrument characterization

4.1 Local oscillator

In this implementation of the TIR LHR, a single fixed filter approach has been retained and the spectral components are obtained through the scanning of the LO frequency. The QCL operating frequency is temperature and current dependent and was studied and measured to ensure control over the emitted laser frequency. The wavenumber σ emitted as function of current and temperature T is modelled by the function given in Eq. (7). This equation describes the quadratic dependence of frequency on both current and temperature, as well as a cross-coupling term between the two tuning parameters. Fitting of the tuning data allows determining the parameters driving Eq. (7). These are given in Table 2 and are used to define the coarse operating point of the laser.

$$\sigma = \sigma_0 + i_1 \cdot I + i_2 \cdot I^2 + t_1 \cdot T + t_2 \cdot T^2 + x \cdot I \cdot T \quad (7)$$

The high stability laser module allows operation from -15°C . The laser has a maximum current of 0.56 A and a maximum operating temperature of 30°C . The laser threshold is 0.36 A at the lowest achievable temperature. Hence, the accessible tuning range is 950.78 to 955.37 cm^{-1} and the laser can access the optimum narrow spectral window at about 953 cm^{-1} determined in the previous section. An operating temperature of 9°C and a DC current of 0.477 A

were chosen. Current tuning is performed using a sawtooth-waveform voltage ramp produced by a function generator that produces a current tuning of $\pm 85 \text{ mA}$.

The laser can deliver up to 20 mW of optical power, and attenuation is necessary to reach the LO power which optimizes the heterodyne SNR ($\sim 150 \mu\text{W}$). Spectral characteristics were analysed using a Bristol wavemeter/spectrum analyser and were found to be single mode throughout the operating range. Spatial profiles were checked to be TEM 00 ellipsoidal Gaussian (residual with Gaussian fit < 5 % of the peak intensity value), with additional signs of residual diffraction from the collimation lens. The beam ellipticity is constantly $\sim 10 \%$ and the M^2 parameter was evaluated to be ~ 1.2 .

4.2 Frequency calibration

As a first approximation, ignoring contributions from potentially interfering lines, the total column is related to the area delimited by a single isolated spectral absorption line. Therefore, the accuracy of the retrieved signal is strongly dependent on the accuracy of the relative frequency calibration of the spectral data. To that end, real-time frequency calibration is conducted using the etalon described in the experimental section, which provides a free spectral range of $491.35 \pm 0.07 \text{ MHz}$ at 953 cm^{-1} and 21°C .

The wavenumber axis associated with a spectral scan is determined by an identical frequency calibration procedure as described by Tsai et al. (2012). A high-order polynomial is fitted to the resulting data from the etalon optical arm, giving the relative laser frequency calibration by steps of half a free spectral range (between two consecutive extrema in the etalon trace). The relative wavenumber vector is shifted to absolute wavenumbers by matching the narrow CO_2 absorption line centre to the corresponding value tabulated in the HITRAN spectral database.

In order to gain insight into the stability of the relative frequency calibration throughout a full day, continuous spectral scans were recorded every 90 s to construct a long dataset of frequency calibration data ($\sim 05:00$ – $19:00$ UTC on 30 June 2015). The raw etalon signals over the full day are shown in Fig. 4a and frequency drifts are clearly perceptible throughout the 14 h measurement period. Frequency drifts are not an issue since they would not affect the relative frequency calibration that is the crucial parameter. As an estimate of the laser frequency change per data point, the derivative of the relative laser calibration function with respect to the sampling point index is used. The initial scan is taken as a reference and subtracted from all the subsequent calibrations to estimate the stability of the frequency spread per point. These data are shown in Fig. 4b. The relative wavenumber calibration appears least reliable near both ends of a scan, where the polynomial fitting is less constrained, in particular where low LO power does not produce clear extrema. Otherwise, when these edge effects are removed, the 1σ statistical spread of the data point spacing is $\sim 0.7 \text{ MHz/point}$ over

Table 2. Laser tuning coefficients corresponding to the model in Eq. (7).

Wavenumber offset (cm^{-1})	$\sigma_0 = 955.90 \pm 0.05$
Linear current tuning coefficient ($\text{cm}^{-1} \text{A}^{-1}$)	$i_1 = -1.71 \pm 0.2$
Quadratic current tuning coefficient ($\text{cm}^{-1} \text{A}^{-2}$)	$i_2 = -5.42 \pm 0.2$
Linear temperature tuning coefficient ($\text{cm}^{-1} \text{K}^{-1}$)	$t_1 = -0.0539 \pm 0.0011$
Quadratic temperature tuning coefficient ($\text{cm}^{-1} \text{K}^{-2}$)	$t_2 = (-5.56 \pm 0.29) \times 10^{-4}$
Current temperature tuning coupling ($\text{cm}^{-1} \text{A}^{-1} \text{K}^{-1}$)	$x = -0.020 \pm 0.002$

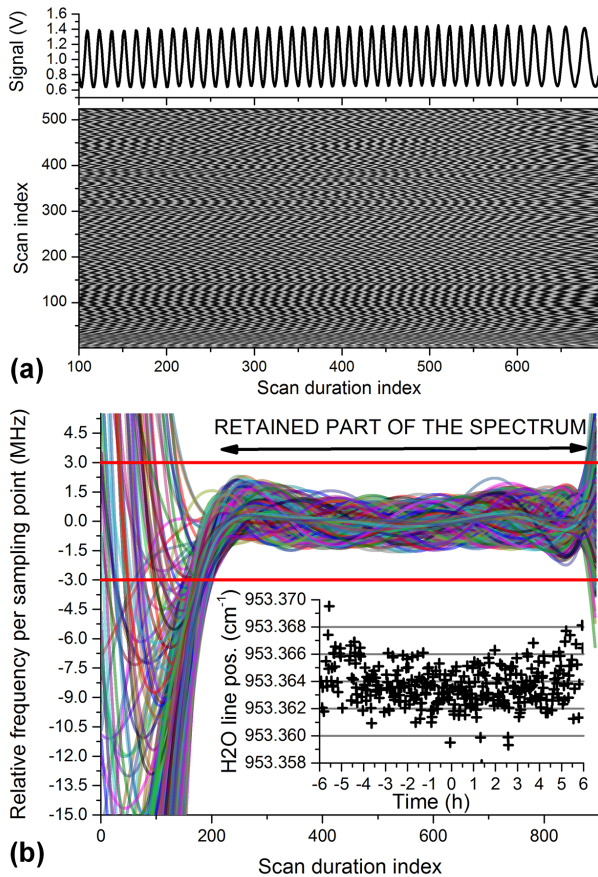


Figure 4. (a) Contour plot showing a subset of successive etalon signals (corrected from envelope power variation, lower panel). The upper panel shows one signal trace; (b) consecutive derivatives of the same day’s measurements’ relative frequency vectors, from which the initial derivative vector has been subtracted to estimate frequency calibration stability. The inset shows the free-floating H_2O spectral line centroid position for the same batch of measurements.

the 14 h period, which is an outstanding stability. To maintain confidence in the frequency calibration, setting a stability requirement of < 3 MHz/point, a daily batch of spectra are automatically trimmed following this methodology to match the 3 MHz/point stability requirement on average.

A perhaps more intuitive method to assess the uncertainty in frequency calibration consists in evaluating the relative

spectral line positions of the H_2O and the CO_2 transitions after calibration (Fig. 4b, inset). To this aim, the peak centroid is determined by fitting Lorentzian line shapes to the H_2O absorbance spectra, and retaining only those centroids where the summed squared residuals of the fit remain below a threshold. For the day used in Fig. 4, this criterion is met for 333 out of 455 spectra; values differ mostly for low Sun elevation angles when lines are saturated and centroids are least reliable. Using the CO_2 transition as a reference, the standard deviation of the H_2O line position thus estimated is 0.0015 cm^{-1} . The median lies around $953.36359 \text{ cm}^{-1}$, and if the line position in HITRAN ($953.36743 \text{ cm}^{-1}$) can be taken as a more reliable reference, this yields a bias of -0.0038 cm^{-1} . Likewise, for the 3029 spectra in the archive passing quality control (QC), spanning 8 months of measurements, 2872 successfully had line centroids fitted, resulting in only a slightly higher standard deviation of 0.0024 cm^{-1} and bias of -0.0043 cm^{-1} . Overall, the frequency calibration essentially remains very stable and no systematic drift is observed.

4.3 LHR instrument performance

In order to characterize the radiometric performance of the LHR, measurements using a calibrated blackbody source are needed. To that end, a miniature cavity blackbody source with an emissivity better than 0.99 was used to fill the LHR input aperture. In this case, the radiometric power P received by the instrument can be calculated and is expressed by Eq. (8) (Weidmann et al., 2007a), where $R(\nu, T_{\text{BB}})$ is the Planck function (spectral radiance) for a blackbody at temperature T_{BB} , and B represents the double side band spectroradiometer resolution. Equation (8) accounts for the polarization sensitivity of the LHR, and for the fact that only a single spatial mode of the received field contributes to the heterodyne signal. It additionally accounts for broadband absorption between the source and the receiver photomixer through a transmission term κ :

$$P = \frac{1}{2} \cdot \kappa \cdot R(\nu T_{\text{BB}}) \cdot \frac{c^2}{\nu^2} \cdot B. \quad (8)$$

Under the ideal limit of a shot-noise-limited LHR, the noise equivalent power (NEP) is expressed by Eq. (9), in which η stands for the heterodyne efficiency of the photomixer, τ the integration time, and h denotes Planck’s constant. From

Eqs. (8) and (9), the theoretical shot-noise-limited SNR of the LHR can be expressed and is given by Eq. (10), in which k is the Boltzmann constant. These equations of NEP and SNR are used to assess the experimental LHR performance when referenced to the ideal shot noise limit. In other words, the SNR expressed by Eq. (10) corresponds to the expected performance of an ideal LHR for which the sole source of noise is shot noise, after all known signal losses up to the detector element have already been factored out.

$$\text{NEP} = \frac{h \cdot \nu}{\eta} \sqrt{\frac{B}{\tau}}, \quad (9)$$

$$\text{SNR} = \frac{\eta \cdot \kappa \cdot \sqrt{B \cdot \tau}}{\exp\left[\frac{h \cdot \nu}{k \cdot T_{\text{BB}}}\right] - 1}. \quad (10)$$

The blackbody temperature is set to $T_{\text{BB}} = 1323 \pm 1.7$ K. Throughout the optical system up to the photomixer the transmission of the blackbody radiation (κ) is 57.4 % (53.5 % when coupled to the solar tracker). For the blackbody, this value combines the optical losses due to seven gold-plated mirrors (0.98 assumed reflectance), LWP (0.90 transmittance), BS (0.75 transmittance) and the ZnSe wedged window in front of PD1 (0.98 transmittance). For the solar radiation, there are three gold-plated mirrors, two silver-plated mirrors (0.98 assumed reflectance), three outdoor gold-plated mirrors (0.98 assumed reflectance, in spite of likely degradation due to exposure), and an additional BaF₂ window below the tracker (0.95 transmittance). The heterodyne efficiency of the photomixer is taken from the quantum efficiency provided by the manufacturer at this wavelength (0.26). It is worth noting that the photomixer is based on a resonant optical cavity design and is not optimized for the ~ 950 cm⁻¹ frequency. When operating in optimized conditions, heterodyne efficiencies of up to 0.5 have been obtained. The LHR double side band spectral resolution is set to 60 MHz, and the integration time to 50 ms. Under these conditions, at fixed LO frequency (2.86×10^{13} Hz or 955 cm⁻¹), the measured SNR is 75, which is only 1.9 smaller than the ideal SNR calculated from Eq. (10). A long temporal record of heterodyne signal was also used for an Allan variance calculation to establish the stability time of the system, which was found to be ~ 100 s (limited by liquid nitrogen-cooled dewar temperature drifts). This quantity underpinned the choice of the integration time.

Next, a similar experiment was run under more realistic conditions of LO frequency scanning. The LO was tuned over ~ 1 cm⁻¹ by a linear current ramp. For this experiment, the LHR double side band spectral resolution was set to 600 MHz. During the tuning process, the LO also exhibits power variation (Fig. 5a). The QCL operating set point was chosen such that the laser is nearly at lasing threshold at the start of the ramp. The evolution of the noise over the course of the tuning can be seen in Fig. 5b. As the laser frequency is scanned, the heterodyne noise increases by ~ 60 % (note that

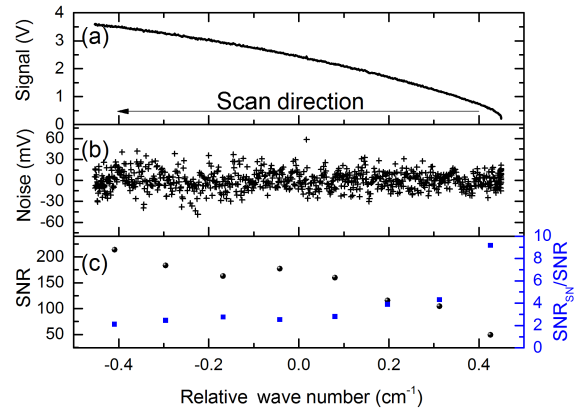


Figure 5. (a) Heterodyne signal change throughout the LO frequency scan (current tuning) using a 1373 K blackbody as a source; (b) heterodyne signal noise over the laser tuning; (c) evolution of the LHR SNR computed on successive chunks of 100 data points. $\text{SNR}_{\text{SNR}} / \text{SNR}$ depicts the ratio of the theoretically calculated shot-noise-limited SNR (Eq. 10) over the measured SNR.

the laser frequency is scanned towards lower frequency as current increases). However, since the increase in LO power boosts the heterodyne signal significantly, the SNR increases and sets at half of the ideal shot-noise-limited SNR (SNR_{SNR}).

5 Atmospheric measurements

5.1 Atmospheric spectra

The LHR has been recording atmospheric transmission spectra since 21 May 2015 and continues to operate whenever the weather allows. Some of the atmospheric transmission spectra recorded with the highest SNR in this period are shown in Fig. 6. Unless otherwise stated, total acquisition time is 90 s. In the previous section, it has been established that the instrument operates within roughly 2 times the ideal shot noise limit. This represents the intrinsic instrument performance independent of any received radiometric signals. However, the absolute SNR also scales with the amount of power received from the source. Therefore, the highest SNR is obtained on days where the broadband atmospheric extinction (primarily due to aerosols) is lowest and the total atmospheric column traversed (set by date and time of day) is shortest. The spectra of Fig. 6 correspond to this situation. The spectral resolution is primarily set by the double side bandwidth B of the RF filter used (60 MHz or 0.002 cm⁻¹ and 600 MHz or 0.02 cm⁻¹ respectively). The RF filters govern the ILS, which has been accurately measured electronically and is convolved with the modelled spectrum. The smoothing effect of a larger ILS on the narrow tip of the CO₂ absorption line is illustrated in the atmospheric spectra of Fig. 6. Lock-in integration time and sampling frequency have been set such that

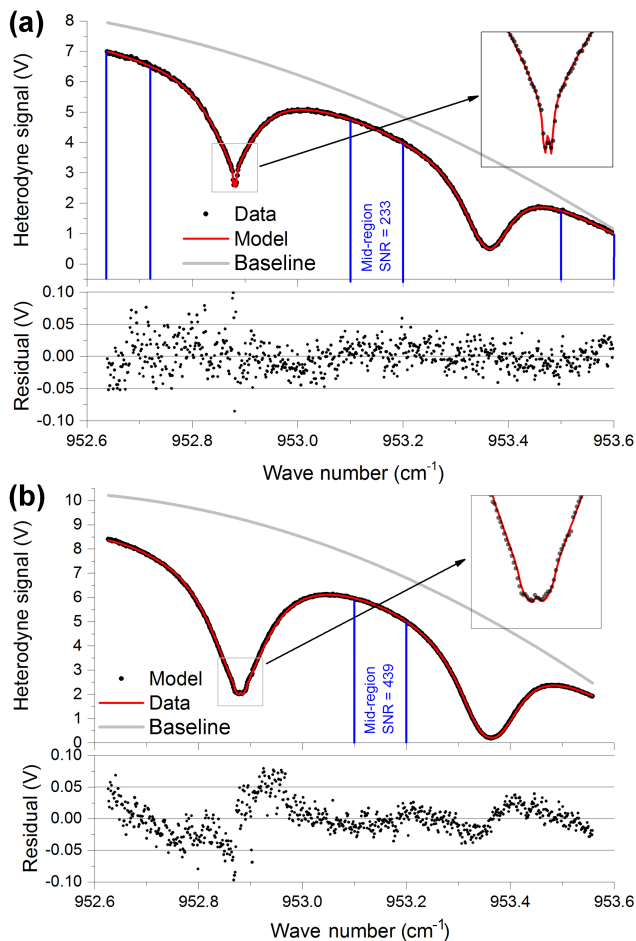


Figure 6. Atmospheric spectra (and modelled fits after retrieval) in the selected window at two spectral resolutions, recorded (a) on 10 September 2015 11:17 UTC at 60 MHz with a midsection SNR of 233 and (b) on 28 September 2015 15:29 UTC at 600 MHz with a midsection SNR of 439. The thin blue lines delimit the spectral window over which the SNR and measurement noise are estimated after applying a second order polynomial fit. The thin grey lines show the polynomial baselines due to LO power change.

the spectral resolution determined by the RF filters is slightly oversampled.

Between 4 June 2015 and 20 January 2016, 6901 spectra have been collected. Semi-automated unsupervised pre-processing (in IDL) is used to load data and metadata, perform the spectral frequency calibration, trim the spectra, remove the broadband power offset, estimate measurement noise and SNR, interpolate the spectra onto a regular grid, compute mean Sun elevation angle, and screen for QC. An initial guess of the polynomial baseline corresponding to the LO power change is also done as an input to the retrieval algorithm. QC is currently based around a set of a priori criteria and thresholds applied to statistical and signal analysis indicators. It is designed to flag up spectra adversely affected by cloud contamination, discontinuous (off-

centred) solar tracker pointing and external noise interference. Screening classification errors have been assessed to remain below roughly 10%. From the 6901 original spectra, 3029 have been retained after QC.

Following the method outlined in Weidmann et al. (2007a), measurement noise σ_{noise} (expressed as a heterodyne signal voltage) and SNR are estimated from the 1σ standard deviation and average signal intensity on discrete subsections of the spectra (upper, middle, and lower; Fig. 6). For each subsection, the piecewise signal is first corrected for baseline variation by a second-order polynomial fit to the data. As mentioned above, the SNR typically decreases from the upper (largest signal) towards the lower part of the spectrum. Within the retrieval algorithm, an average of the noise across the three values is currently introduced. Hereafter, the focus is on the most representative midsection. Since measurements have been recorded with different filter bandwidths (spectral resolutions) and integration times, SNR and noise are normalized by $\sqrt{B \cdot \tau}$ and $\sqrt{B/\tau}$, respectively, following Eqs. (10) and (9), to characterize the instrument's spectroradiometric performance independently of instrument settings. These normalized values, for the entire archive of 3029 valid measurements, are plotted in Fig. 7a and b, colour-coded according to the acquisition day.

Besides a set of outliers corresponding to the most recent measurements in January, all noise measurements collapse neatly around a median value of $\sim 3 \times 10^{-7} \text{ mV Hz}^{-1}$, independently of date and time (Fig. 7b). This noise level inherently characterizes the LHR as an instrument, independently of any received radiometric signal. Conversely, since the SNR varies linearly with signal magnitude, and since the latter is highly dependent on the atmospheric state and the Sun's position, the SNR (Fig. 7a) predominantly reflects environmental conditions. The SNR strongly varies on a seasonal basis, changes with the atmosphere's broadband extinction and cloud cover, and on an otherwise clear-sky day (30 June 2015, red circles), follows a distinctive diurnal pattern. Some sequences exhibit extreme measurement-to-measurement variability; this is most likely due to fractional cloud cover with a large amount of high-altitude cirrus (Ci) and haze, which reduces the signal without blocking it owing to the reduced scattering in the TIR. On 11 September 2015 (orange stars), for example, SNR and solar broadband are strongly correlated ($\rho = 0.88$), and the latter, characterizing cloud cover, heavily fluctuates in time.

By converting the noise-level heterodyne voltage into radiometric power units, the normalized NEP can directly be compared to a normalized version of the theoretical shot noise limit from Eq. (9), i.e. $h\nu/\eta$. Therefore, an instrument calibration curve, mapping heterodyne voltage into radiometric power (radiant flux) units, was established. Towards its low-power end, this curve was constructed by recording heterodyne voltages for cavity blackbody measurements with temperatures varying between 373 and 1323 K, and using Eq. (8) to model the associated radiant flux, assuming an

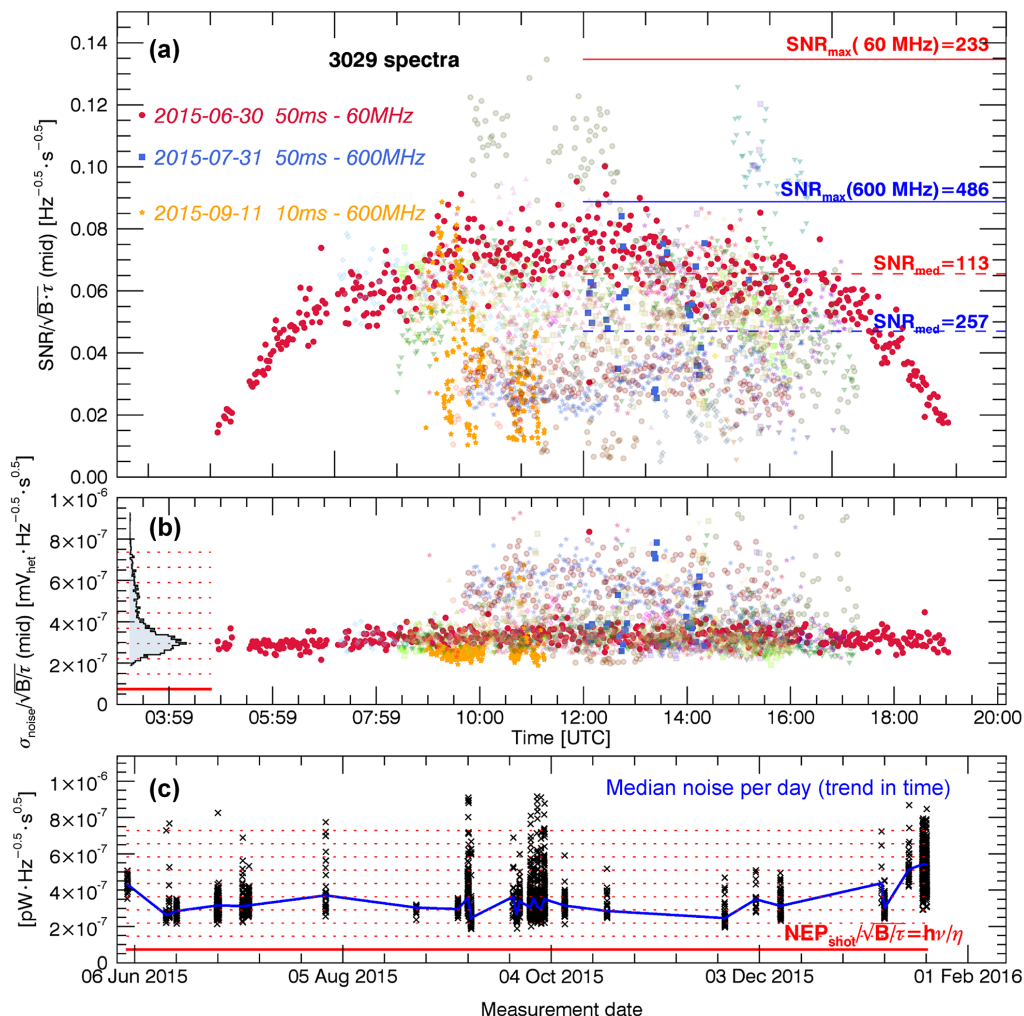


Figure 7. LHR radiometric performance analysis over the full archive of quality-controlled spectra. Only the three most relevant measurement dates for the analysis are given in the legend to improve clarity. **(a)** Normalized (see text for details) midsection ($953.15 \pm 0.05 \text{ cm}^{-1}$) SNR; the maximum and median SNR text values from the entire measurement series are not normalized, but their locations (horizontal lines) in the plot are. **(b)** Normalized midsection measurement noise in heterodyne voltage units (i.e. factoring out lock-in amplifier sensitivity settings). The noise is estimated as 1 standard deviation of the midsection signal segment, corrected for the baseline variation. The histogram on the left shows the corresponding statistical distribution, **(c)** Normalized noise converted into a radiant flux (see text) as a function of date and time of measurement. Black crosses correspond to the same individual measurements as in **(b)**, but plotted on a running time axis; occasionally, the scatter within a single day is large, although measurements mostly clump around a similar value (see median curve). The red solid and broken lines correspond to the theoretical shot noise limit and consecutive multiples thereof.

emissivity of 1. Thereafter, for the high-power end, the solar signal was coupled back into the instrument, introducing an unknown radiant flux. Using $23 \mu\text{m}$ Mylar[®] polyester sheets as known attenuators (previously characterized by FTIR measurements), the measured heterodyne signal received was lowered until it reaches the domain covered by the laboratory blackbody calibration, hence calibrating the unknown radiance received by the instrument. Attenuating sheets were subsequently removed one by one to produce calibration points. The radiometric calibration curve was found to be linear. The intercept was forced to zero and the slope

was measured to be $G_{v2r} = 0.989 \pm 0.008 \text{ pW mV}^{-1}$, considering the blackbody measurements only.

Using the radiometric calibration gain, the normalized NEP can be calculated from the data shown in Fig. 7b. These are plotted in Fig. 7c, but this time as a function of measurement date and time. The median noise level exceeds the shot noise limit by roughly a factor of 4. Measurement noise did not significantly drift in time over the 8 months of operation, besides an unexplained sharp increase in January 2016, currently attributed to observed excess low frequency electrical signal picked up by the detection chain. Compared to

the previously established factor of 2 for blackbody measurements, the most likely candidate for this additional performance degradation is broadband thermal noise that is not rejected by the RF filter. This hypothesis is strengthened by the observation that noise seems to increase with the radiant flux received. Future use of a narrower bandpass filter may remediate this issue. Nevertheless, the system consistently operates close to the shot noise limit, highlighting the excellent radiometric performance of the LHR.

High- and medium-altitude optically thin clouds (cirrus and some altocumulus) were often found to be transparent enough in the thermal infrared to allow the LHR to collect spectra. The narrow FOV and the high temporal resolution of the LHR, combined with the passive tracking approach, allows the capture of data not only through the clear sky between patchy clouds but also through thin clouds, as can be seen in Fig. 8a, in which a picture of the sky at the time of measurement is also shown. Obviously, the signal attenuation due to clouds lowers the SNR, but information can nevertheless be obtained. During the acquisition time of the spectra, (90 s in this particular case), one needs to ensure that cloud attenuation variation will not create spectral artefacts. The broadband NIR solar intensity signal can be used to determine whether this condition is fulfilled, although the non-linear influence of clouds on radiative transfer (Fig. 8a, inset) warrants the exercise of caution. For a specific example, Fig. 8a, inset, shows a fixed frequency temporal record of both the heterodyne signal and the broadband NIR solar intensity signal as clouds were passing through the LHR's line of sight. Within the linearity region (broadband NIR signal > 0.1 V), while the NIR infrared broadband signal is reduced 6 fold, the heterodyne signal decreases by only a factor of ~ 1.3 .

A field- or space-deployable TIR LHR should eventually utilize a thermoelectrically cooled (TEC) as opposed to a cryogenically cooled photomixer. To close this technical study, a proof-of-concept atmospheric spectrum with a TEC detector (Vigo PV-4TE-10 with a custom preamplifier) is shown in Fig. 8b, in comparison to an equivalent spectrum with the liquid nitrogen-cooled photomixer. The narrower bandwidth of the TEC detector (~ 50 – 100 MHz single side bandwidth, in conjunction with the 50 – 350 MHz RF filter), apparent from the sharper CO_2 absorption peak, needs to be accounted for when comparing the performance of both in terms of NEP. After factoring in this difference, it appears that the TEC detector only underperforms the cryogenically cooled photomixer by a factor of roughly 2. It is anticipated that more advanced detector arrangements will improve this performance even further.

5.2 Towards retrievals

Ultimately, low measurement noise should translate into the small uncertainty required for CO_2 flux inversions and carbon cycle studies, provided all biases can be accounted and

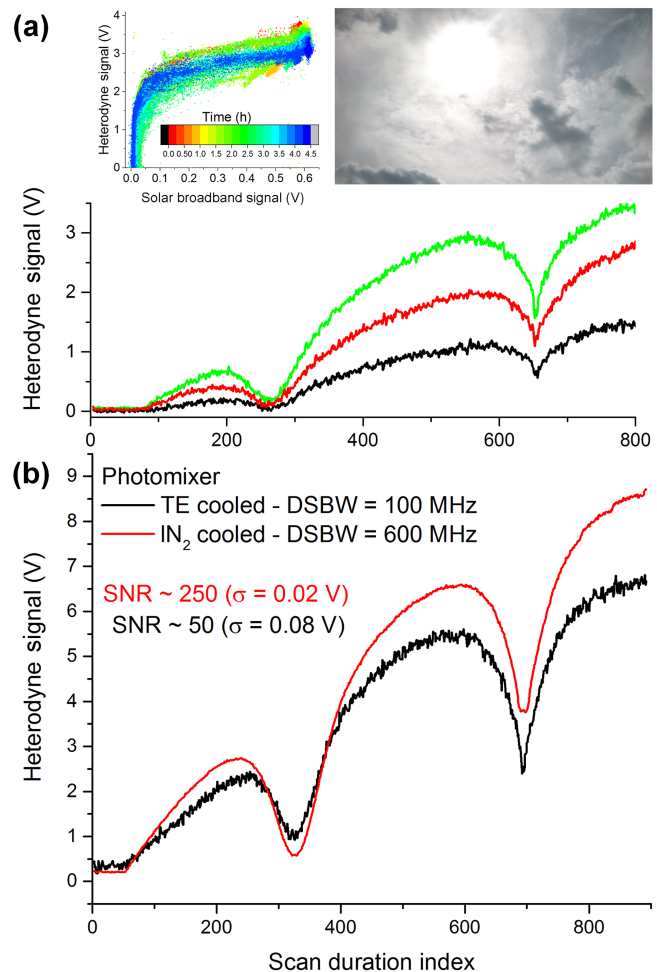


Figure 8. (a) LHR atmospheric spectra recorded for three different levels of cloud attenuation (at 60 MHz spectral resolution and with 50 ms integration time). The insets show a picture of the sky during the measurements and a scatterplot of NIR solar broadband versus heterodyne signal, constructed using a number of constant frequency recordings with variable cloud amounts and types. (b) Spectra obtained with two different types of photomixers. The liquid N_2 -cooled photomixer with 600 MHz double side bandwidth has primarily been used for this work and is compared to a thermoelectrically (Peltier) cooled photodiode with 100 MHz double band bandwidth (approximate measured detector bandwidth is 100 MHz, giving a SSBW of 50–100 MHz after convolution with the RF filter).

corrected for. Bias analysis, a detailed description of the retrieval scheme, its configuration, optimization, and validation, are beyond the scope of this study and are subject to follow-on work. However, in order to characterize the instrument error propagation and the associated measurement precision and to demonstrate the approach, preliminary retrievals have been run on some of the screened and pre-processed data collected on 30 June 2015.

The retrieval algorithm remains the same as that used as OSS, with synthetic spectra replaced by real measurements. Input temperature and pressure profiles from the MIPAS mid-latitude reference atmosphere have been substituted up to a height of ~ 15 km by operational radiosonde data, acquired at 09:00 UTC on the measurement day from station 3743 (51.20° N, 1.80° W). The CO₂ a priori profile was in a first instance simply set to a constant 400 ppm VMR up to 30 km altitude, with arbitrarily chosen uncertainties of 50, 30, 10, and 50 ppm at 0.4, 2, 10, and 30 km retrieval grid altitude, respectively, reflecting large variability in the PBL and an unknown concentration in the stratosphere. In reality, CO₂ climatologies, stratospheric age of air empirical models from in situ measurements, and chemistry transport models imply that stratospheric CO₂ decreases with height above the tropopause (Andrews et al., 2001; Chatterjee et al., 2013; Saito et al., 2011; Wunch et al., 2011); in future algorithm iterations, the x_a profile and associated uncertainties should reflect a better-constrained state and its variability. The S_a block matrix corresponding to CO₂ was further constructed using an approximate and coarse interpolation of the CO₂ correlation matrix given in O'Dell et al. (2012) (their Fig. 2) onto the retrieval grid, in order to constrain the retrieved profile to a smoother vertical shape. A relative error of 50 % was assigned to all the levels (0.3, 1.5, 3, and 8 km) of the prior H₂O profile and of 100 % to the three coefficients describing the second order polynomial baseline (RADSCALE) accounting for LO power variation and broadband atmospheric attenuation. Off-diagonal terms on S_a corresponding to H₂O and the baseline were all set to 0, as were those on the instrument noise covariance matrix S_e . Note that a priori profiles and uncertainties do not currently represent suitable inputs to produce reliable geophysical output and will eventually need to be determined from appropriate climatologies and re-analysis data, as emphasized above. The algorithm solution is defined to have converged when $\Delta\chi^2/\chi^2 < 0.001$, within an upper limit of 10 iterations.

Preliminary retrieval results are shown in Fig. 9; only a subset of inversions complying with an arbitrary threshold of χ^2/m of 2 (Eq. 1), where m is the number of sampling points, have been retained. The total column-averaged mole fraction of CO₂ (in dry air), TC_{CO₂} (X_{CO_2}), remains relatively stable over the course of a day (Fig. 9b), in particular when a nine-point smoothing filter (moving average) is computed over individual data points obtained from 90 s measurements. The daytime average X_{CO_2} measured was 395.85 ppm, which is roughly consistent with GOSAT (interpolated) FTS SWIR L3 data over the UK (~ 400 and $\sim 396 \pm 2$ ppm (standard error) on average for months of June and July 2015 respectively). Obviously, this comparison is not meant to serve as a validation argument; rather, it merely provides a rough reality check on the retrieved quantities.

A slight upwards trend is observed in the smoothed X_{CO_2} measurement series in Fig. 9b, which could represent, but not necessarily is, a real feature. The individual measurements

have been de-trended by subtracting the moving average; the standard deviation across this de-trended time series is 2.6 ppm. This exceeds the total column retrieval uncertainty (from instrument error propagation) of ~ 1.5 ppm (see below). Assuming that X_{CO_2} might remain reasonably constant over a period of ~ 15 –30 min, the approximate smoothing period of the moving average over the (thinned) dataset, this hints at further error sources not included in the retrieval error propagation. This warrants further investigations, though we anticipate that a more carefully optimized set of retrieval parameters, including of the retrieval grid, more rigorous atmospheric input profiles, and possibly improvements in the spectroscopic parameters, might improve these figures.

The uncertainty on X_{CO_2} from error propagation (1.9 ppm for a 90 s measurement at 60 MHz resolution) comprises a contribution from the (arbitrarily chosen) uncertainty on surface pressure of 3 hPa. If the latter is ignored to capture only instrumental error propagation, the uncertainty on X_{CO_2} mirrors that of TC_{CO₂}, estimated to be ~ 1.5 ppm. As already mentioned, no systematic errors or bias analysis is included at this stage. This uncertainty is just above two times worse compared to that obtained using the OSS at 60 MHz resolution (0.7 ppm) and within the requirements of CO₂ flux inversion modelling studies. The comparison has to be treated with caution as the OSS used to identify optimum sounding narrow windows was constrained with a larger a priori uncertainty (20 % relative error on all levels) and without covariance terms on S_a . We anticipate these uncertainty figures to be improved by increasing the SNR of the recorded spectra (higher spectral resolution and/or longer integration time than 90 s). Introducing more rigorous a priori profiles from climatologies, with adequately characterized covariance matrices is also in the scope of follow-on improvements. Here, the large covariance terms introduced in S_a for CO₂, meant to smoothen the profile by emulating large-scale free tropospheric vertical mixing, obviously shifts the dominant error contribution from measurement error in the OSS (Fig. 2a) to smoothing error (Fig. 9a).

The water vapour total column is better suited for a straight side-by-side comparison between the OSS and actual measurement instrumental error propagation. In both cases, a priori constraints were identical. The OSS indicated a 1 % relative error on TC_{H₂O}, whilst the measurements are at a 5 % relative error level, compared to the 50 % relative error assigned to the prior humidity profile on all state vector altitudes. Although a difference by a factor of 5 appears consistent with the average noise degradation of real measurements compared to the shot noise limit (~ 4), this comparison is not straightforward, given different humidity profiles and different (and dominant) smoothing error contributions, particularly in the boundary layer.

Unlike total columns, vertical profiling is, unsurprisingly given the a priori, under-constrained and shows unphysical oscillations. Follow-on work will focus on addressing these

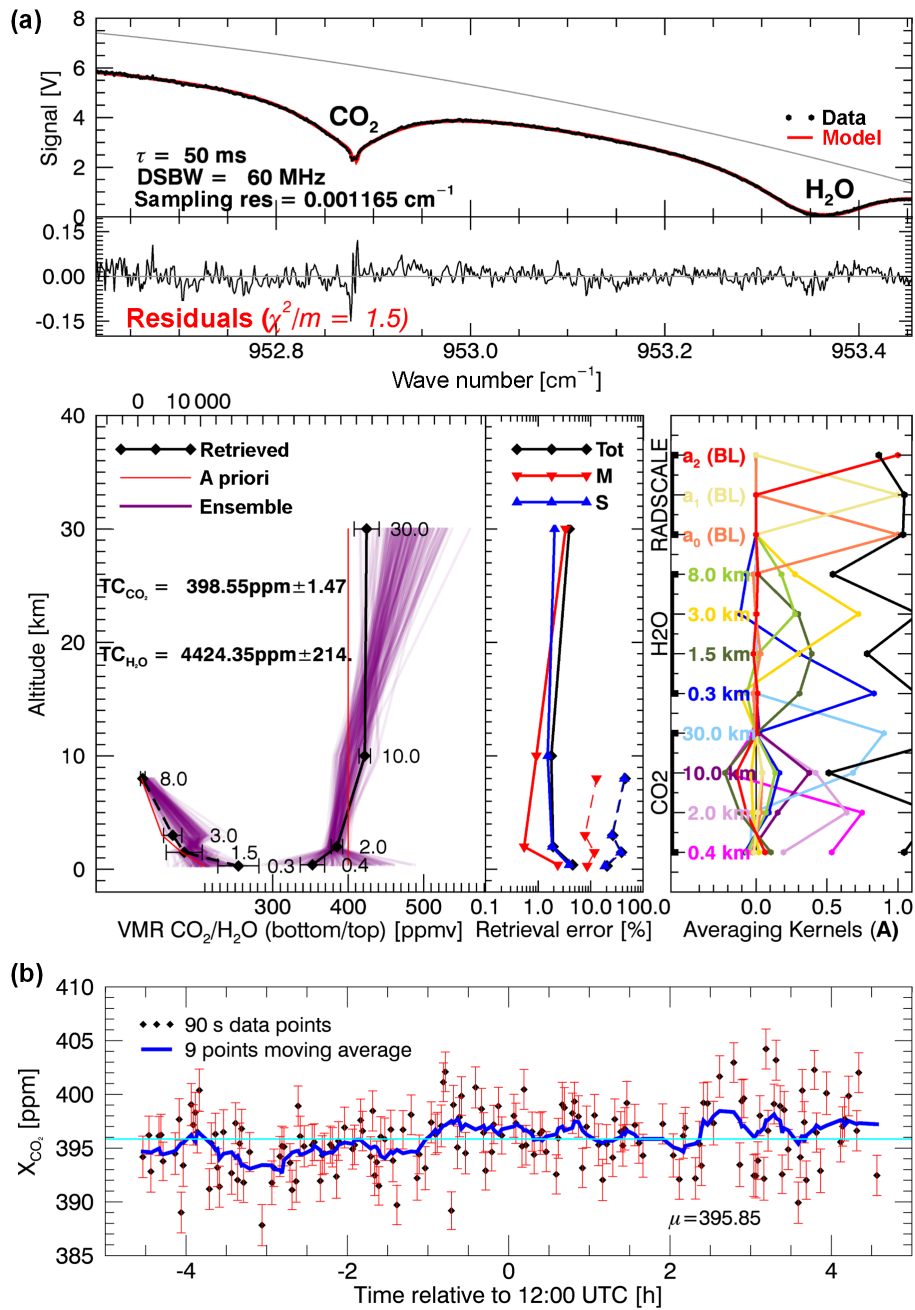


Figure 9. Retrieval results for measurements acquired on 30 June 2016 at 60 MHz spectral resolution; only the 166 out of 455 retrievals that converged within 10 iterations and where $\chi^2/m < 2$ have been retained. (a) Same as Fig. 2 but for real data and with different prior conditions (see text). Purple profiles correspond to the ensemble of retained inversions (CO₂ on the right, H₂O on the left); the selected profile (black with error bars corresponding to the retrieval uncertainty) corresponds to a measurement at 12:05 UTC. The top panel shows the measured spectrum (data) with a superimposed retrieved spectrum (model), and the difference is shown as residuals below. The estimated total columns (TC) with uncertainties are given as text. Total retrieval errors (Tot) and contributions from measurement noise (M) and smoothing error (S) are shown as profiles in the centre (solid line for CO₂, broken line for H₂O). The averaging kernels for the composite state vector are shown on the right. The partial DFS in this retrieval configuration, averaged over the series, are 2.4 for CO₂ and 2.0 for H₂O. RADSCALE denotes the instrument baseline (BL); (b) associated daily evolution of X_{CO₂} and moving average computed over the individual retrievals.

issues to better condition the inversion process using valid a priori and improved geophysical inputs.

6 Conclusions and future work

This paper reports the technical development, demonstration and performance assessment of a benchtop prototype thermal infrared (953.1 cm^{-1}) quantum cascade LHR coupled to a passive Sun tracker designed specifically for total column and vertical profile measurements of CO_2 in solar occultation configuration. An observing system simulator was used to estimate the potential performance and define an optimum narrow spectral window to be used by the instrument. Data from over 8 months of operation in 2015 near Chilton, UK, confirm that atmospheric measurements with noise levels down to ~ 4 times the shot noise limit can consistently be achieved. This provides the opportunity for taking very high spectral resolution (here, $60\text{ MHz}/0.002\text{ cm}^{-1}$ and $600\text{ MHz}/0.02\text{ cm}^{-1}$, corresponding to resolving powers of $\sim 500\,000$ and $\sim 50\,000$) measurements with high SNRs (median of 113 at 60 MHz, median of 257 at 600 MHz) at a relatively high temporal resolution (here, 90 s). Spectral information is recorded over a narrow spectral window of $\sim 1\text{ cm}^{-1}$, focusing on the joint measurement of water and CO_2 ro-vibrational transition lines to enable the conversion of the total column-averaged CO_2 mixing ratio into a dry air equivalent. A narrow window, conversely, limits the risks of cross-talk by other trace gases, and single transitions make spectroscopic error relatively easy to deal with. Preliminary retrieval results aiming to investigate the instrumental error propagation into total column-averaged mixing ratios show an X_{CO_2} error in the range of 1–1.5 ppm. Biases and error propagation from geophysical inputs have not been considered yet.

The demonstrated instrumental error reveals that the LHR promises to provide good quality X_{CO_2} data in relation to satellite data validation and carbon cycle studies, especially as the current instrument's performance can be improved through longer integration times and improved detection schemes.

The inherently narrow FOV of a LHR, combined with short acquisition times, was found to increase the probability of collecting unobstructed spectra on cloudy days. Owing to operation in the TIR, signals with clear spectral signatures can still be acquired through optically thin clouds (cirrus) and haze, although at the cost of a reduced SNR in line with the additional attenuation.

From this first demonstration and instrumental assessment, several pieces of follow-on work are required. On the data retrieval side, thorough algorithm characterization and sensitivity (e.g. through input perturbation) studies are needed, alongside more rigorously chosen auxiliary and a priori data to improve the retrieval of, and confidence in, the CO_2 profiles and total column amounts and uncertainties. This in-

cludes comprehensive error and bias evaluation, validation through cross-comparison with collocated and simultaneous measurements with other ground-based remote sensing and in situ instruments as well as satellite and/or airborne observations, and retrievals with other independent algorithms. In a next iteration of the retrieval algorithm, atmospheric broadband attenuation will also tentatively be extracted as a by-product. The development of an operational retrieval scheme will require a number of incremental improvements to refine the algorithm and could follow steps similar to those taken for the TCCON network.

On the instrument development side, the full TIR LHR potential is to be realized through size reduction and engineering into a compact, rugged, and autonomous package for increased portability to ease field deployment. Miniaturization has already started using hollow waveguide hybrid optical integration (Weidmann et al., 2011b) to open up the path towards incorporation of the TIR LHR into dense and large-scale autonomous instrument networks and deployment on air- or spaceborne platforms.

7 Code and data availability

Code and data are not yet formatted into an operational package. Currently available versions are available upon direct request to the authors. In the future, once properly formatted with inclusion of quality assurance parameters and relevant metadata, they may be made available through for example the British Atmospheric Data Centre.

Author contributions. A. Hoffmann prepared the manuscript, operated and contributed to the development of the instrument and its software, wrote and upgraded new data pre-processing and existing retrieval source code, and performed the simulations and data analysis. N. A. Macleod performed the characterization and testing of the instrument and contributed to the manuscript, instrument operation, and data analysis, and gave expert advice throughout the project. M. Huebner designed and assembled the first optical layout of the breadboard and of a new laser cooling system and performed the characterization of the local oscillator. D. Weidmann conceived the instrument and study, designed the solar tracker, contributed to the data analysis and manuscript, and provided technical lead throughout the project. All authors revised and approved the manuscript.

Acknowledgements. This work was supported through a Centre for EO Instrumentation and Space Technology (CEOI-ST) grant (contract no. RP10G0327C20). The authors wish to thank Gary Williams at RAL Space for his technical assistance and contributions to the design, development, and implementation of the solar tracking system, and Jolyon Reburn for revising the manuscript and the members from the Remote Sensing Group for help and useful discussions. A part of the solar tracker control software was built around an open-source Sun position LabVIEW application written at the CRP Henri Tudor, Luxembourg; radiosonde data

were downloaded through the University of Wyoming web portal. The authors thank the anonymous reviewers for their helpful and supportive comments that improved the manuscript, as well as Dietrich Feist and Frank Hase (the editor) for providing useful insights into TCCON.

Edited by: F. Hase

Reviewed by: three anonymous referees

References

- Abbas, M. M., Kunde, V. G., Mumma, M. J., Kostiuk, T., Buhl, D., and Frerking, M. A.: Stratospheric sounding by infrared heterodyne spectroscopy, *J. Geophys. Res.-Space*, 84, 2681–2690, doi:10.1029/JA084iA06p02681, 1979.
- Abshire, J. B., Riris, H., Allan, G. R., Weaver, C. J., Mao, J., Sun, X., Hasselbrack, W. E., Kawa, S. R., and Biraud, S.: Pulsed airborne lidar measurements of atmospheric CO₂ column absorption, *Tellus B*, 62, 770–783, doi:10.1111/j.1600-0889.2010.00502.x, 2010.
- Andrews, A. E., Boering, K. A., Daube, B. C., Wofsy, S. C., Loewenstein, M., Jost, H., Podolske, J. R., Webster, C. R., Herman, R. L., Scott, D. C., Flesch, G. J., Moyer, E. J., Elkins, J. W., Dutton, G. S., Hurst, D. F., Moore, F. L., Ray, E. A., Romashkin, P. A., and Strahan, S. E.: Mean ages of stratospheric air derived from in situ observations of CO₂, CH₄, and N₂O, *J. Geophys. Res.-Atmos.*, 106, 32295–32314, doi:10.1029/2001JD000465, 2001.
- Blanc, P. and Wald, L.: The SG2 algorithm for a fast and accurate computation of the position of the Sun for multi-decadal time period, *Sol. Energy*, 86, 3072–3083, doi:10.1016/j.solener.2012.07.018, 2012.
- Blanco-Muriel, M., Alarcón-Padilla, D. C., López-Moratalla, T., and Lara-Coira, M.: Computing the solar vector, *Sol. Energy*, 70, 431–441, doi:10.1016/S0038-092X(00)00156-0, 2001.
- Boesch, H., Baker, D., Connor, B., Crisp, D., and Miller, C.: Global Characterization of CO₂ Column Retrievals from Shortwave-Infrared Satellite Observations of the Orbiting Carbon Observatory-2 Mission, *Remote Sens.*, 3, 270–304, doi:10.3390/rs3020270, 2011.
- Butz, A., Guerlet, S., Hasekamp, O., Schepers, D., Galli, A., Aben, I., Frankenberg, C., Hartmann, J.-M., Tran, H., Kuze, A., Keppel-Aleks, G., Toon, G., Wunch, D., Wennberg, P., Deutscher, N., Griffith, D., Macatangay, R., Messerschmidt, J., Notholt, J., and Warneke, T.: Toward accurate CO₂ and CH₄ observations from GOSAT, *Geophys. Res. Lett.*, 38, L14812, doi:10.1029/2011GL047888, 2011.
- Chatterjee, A., Engelen, R. J., Kawa, S. R., Sweeney, C., and Michalak, A. M.: Background error covariance estimation for atmospheric CO₂ data assimilation, *J. Geophys. Res.-Atmos.*, 118, 10140–10154, doi:10.1002/jgrd.50654, 2013.
- Chevallier, F., Maksyutov, S., Bousquet, P., Bréon, F.-M., Saito, R., Yoshida, Y., and Yokota, T.: On the accuracy of the CO₂ surface fluxes to be estimated from the GOSAT observations, *Geophys. Res. Lett.*, 36, L19807, doi:10.1029/2009GL040108, 2009.
- Chevallier, F., Deutscher, N. M., Conway, T. J., Ciais, P., Ciattaglia, L., Dohe, S., Fröhlich, M., Gomez-Pelaez, A. J., Griffith, D., Hase, F., Haszpra, L., Krummel, P., Kyrö, E., Labuschagne, C., Langenfelds, R., Machida, T., Maignan, F., Matsueda, H., Morino, I., Notholt, J., Ramonet, M., Sawa, Y., Schmidt, M., Sherlock, V., Steele, P., Strong, K., Sussmann, R., Wennberg, P., Wofsy, S., Worthy, D., Wunch, D., and Zimnoch, M.: Global CO₂ fluxes inferred from surface air-sample measurements and from TCCON retrievals of the CO₂ total column, *Geophys. Res. Lett.*, 38, L24810, doi:10.1029/2011GL049899, 2011.
- Chevallier, F., Palmer, P. I., Feng, L., Boesch, H., O'Dell, C. W., and Bousquet, P.: Toward robust and consistent regional CO₂ flux estimates from in situ and spaceborne measurements of atmospheric CO₂, *Geophys. Res. Lett.*, 41, 1065–1070, doi:10.1002/2013GL058772, 2014.
- Ciais, P., Dolman, A. J., Dargaville, R., Barrie, L., Bombelli, A., Butler, J., Canadell, P., and Moriyama, T.: GEO Carbon Strategy, GEO Secretariat/FAO, Geneva, Switzerland & Rome, Italy, 48 pp., 2010.
- Ciais, P., Sabine, C., Bala, G., Bopp, L., Brovkin, V., Canadell, J., Chhabra, A., DeFries, R., Galloway, J., Heimann, M., Jones, C., Le Quéré, C., Myneni, R. B., Piao, S., and Thornton, P.: Carbon and Other Biogeochemical Cycles, in: *Climate Change 2013: The Physical Science Basis. Contribution of Working Group I to the Fifth Assessment Report of the Intergovernmental Panel on Climate Change*, edited by: Stocker, T., Qin, D., Plattner, G.-K., Tignor, M., Allen, S. K., Boschung, J., Nauels, A., Xia, Y., Bex, V., and Midgley, P. M., Cambridge University Press, Cambridge, United Kingdom and New York, NY, USA, available at: <http://www.ipcc.ch/report/ar5/wg1/> (last access: 12 October 2015), 2013.
- Clarke, G. B., Wilson, E. L., Miller, J. H., and Melroy, H. R.: Uncertainty analysis for the miniaturized laser heterodyne radiometer (mini-LHR) for the measurement of carbon dioxide in the atmospheric column, *Meas. Sci. Technol.*, 25, 55204, doi:10.1088/0957-0233/25/5/055204, 2014.
- Conway, T. J., Tans, P. P., Waterman, L. S., Thoning, K. W., Kitzis, D. R., Masarie, K. A., and Zhang, N.: Evidence for interannual variability of the carbon cycle from the National Oceanic and Atmospheric Administration/Climate Monitoring and Diagnostics Laboratory Global Air Sampling Network, *J. Geophys. Res.-Atmos.*, 99, 22831–22855, doi:10.1029/94JD01951, 1994.
- Crevoisier, C., Sweeney, C., Gloor, M., Sarmiento, J. L., and Tans, P. P.: Regional US carbon sinks from three-dimensional atmospheric CO₂ sampling, *P. Natl. Acad. Sci. USA*, 107, 18348–18353, doi:10.1073/pnas.0900062107, 2010.
- Crisp, D., Atlas, R. M., Breon, F.-M., Brown, L. R., Burrows, J. P., Ciais, P., Connor, B. J., Doney, S. C., Fung, I. Y., Jacob, D. J., Miller, C. E., O'Brien, D., Pawson, S., Randerson, J. T., Rayner, P., Salawitch, R. J., Sander, S. P., Sen, B., Stephens, G. L., Tans, P. P., Toon, G. C., Wennberg, P. O., Wofsy, S. C., Yung, Y. L., Kuang, Z., Chudasama, B., Sprague, G., Weiss, B., Pollock, R., Kenyon, D., and Schroll, S.: The Orbiting Carbon Observatory (OCO) mission, *Adv. Space Res.*, 34, 700–709, doi:10.1016/j.asr.2003.08.062, 2004.
- Deng, F., Jones, D. B. A., Henze, D. K., Bousserrez, N., Bowman, K. W., Fisher, J. B., Nassar, R., O'Dell, C., Wunch, D., Wennberg, P. O., Kort, E. A., Wofsy, S. C., Blumenstock, T., Deutscher, N. M., Griffith, D. W. T., Hase, F., Heikkinen, P., Sherlock, V., Strong, K., Sussmann, R., and Warneke, T.: Inferring regional sources and sinks of atmospheric CO₂ from GOSAT XCO₂ data,

- Atmos. Chem. Phys., 14, 3703–3727, doi:10.5194/acp-14-3703-2014, 2014.
- Deutscher, N. M., Griffith, D. W. T., Bryant, G. W., Wennberg, P. O., Toon, G. C., Washenfelder, R. A., Keppel-Aleks, G., Wunch, D., Yavin, Y., Allen, N. T., Blavier, J.-F., Jiménez, R., Daube, B. C., Bright, A. V., Matross, D. M., Wofsy, S. C., and Park, S.: Total column CO₂ measurements at Darwin, Australia – site description and calibration against in situ aircraft profiles, *Atmos. Meas. Tech.*, 3, 947–958, doi:10.5194/amt-3-947-2010, 2010.
- Dudhia, A.: Reference Forward Model (RFM) Software User's Manual, ESA Document, Noordwijk, available at: www.atm.ox.ac.uk/RFM/ (last access: 7 September 2015), 1997.
- Dudhia, A.: The Reference Forward Model (RFM), *J. Quant. Spectrosc. Ra.*, 186, 243–253, doi:10.1016/j.jqsrt.2016.06.018, 2017.
- Fast, K. E., Kostiuk, T., Espenak, F., Livengood, T. A., Hewagama, T., and A'Hearn, M. F.: Stratospheric ozone profiles from Mauna Kea, Hawai'i (19.8° N, 155.5° W) using infrared heterodyne spectroscopy, 1988–2003, *Geophys. Res. Lett.*, 31, L08109, doi:10.1029/2004GL019443, 2004.
- Frerking, M. A. and Muehlnher, D. J.: Infrared heterodyne spectroscopy of atmospheric ozone, *Appl. Opt.*, 16, 526–528, doi:10.1364/AO.16.000526, 1977.
- Gerbig, C., Lin, J. C., Wofsy, S. C., Daube, B. C., Andrews, A. E., Stephens, B. B., Bakwin, P. S., and Grainger, C. A.: Toward constraining regional-scale fluxes of CO₂ with atmospheric observations over a continent: 1. Observed spatial variability from airborne platforms, *J. Geophys. Res.-Atmos.*, 108, 4756, doi:10.1029/2002JD003018, 2003.
- Gibert, F., Flamant, P. H., Cuesta, J., and Bruneau, D.: Vertical 2- μ m Heterodyne Differential Absorption Lidar Measurements of Mean CO₂ Mixing Ratio in the Troposphere, *J. Atmos. Ocean. Tech.*, 25, 1477–1497, doi:10.1175/2008JTECHA1070.1, 2008.
- Gisi, M., Hase, F., Dohe, S., and Blumenstock, T.: Camtracker: a new camera controlled high precision solar tracker system for FTIR-spectrometers, *Atmos. Meas. Tech.*, 4, 47–54, doi:10.5194/amt-4-47-2011, 2011.
- Glenar, D., Kostiuk, T., Jennings, D. E., Buhl, D., and Mumma, M. J.: Tunable diode-laser heterodyne spectrometer for remote observations near 8 μ m, *Appl. Opt.*, 21, 253–259, doi:10.1364/AO.21.000253, 1982.
- Grena, R.: Five new algorithms for the computation of sun position from 2010 to 2110, *Sol. Energy*, 86, 1323–1337, doi:10.1016/j.solener.2012.01.024, 2012.
- Gurney, K. R., Law, R. M., Denning, A. S., Rayner, P. J., Baker, D., Bousquet, P., Bruhwiler, L., Chen, Y.-H., Ciais, P., Fan, S., Fung, I. Y., Gloor, M., Heimann, M., Higuchi, K., John, J., Maki, T., Maksyutov, S., Masarie, K., Peylin, P., Prather, M., Pak, B. C., Randerson, J., Sarmiento, J., Taguchi, S., Takahashi, T., and Yuen, C.-W.: Towards robust regional estimates of CO₂ sources and sinks using atmospheric transport models, *Nature*, 415, 626–630, doi:10.1038/415626a, 2002.
- Houweling, S., Baker, D., Basu, S., Boesch, H., Butz, A., Chevalier, F., Deng, F., Dlugokencky, E. J., Feng, L., Ganshin, A., Hasekamp, O., Jones, D., Maksyutov, S., Marshall, J., Oda, T., O'Dell, C. W., Oshchepkov, S., Palmer, P. I., Peylin, P., Poussi, Z., Reum, F., Takagi, H., Yoshida, Y., and Zhuravlev, R.: An intercomparison of inverse models for estimating sources and sinks of CO₂ using GOSAT measurements, *J. Geophys. Res.-Atmos.*, 120, 5253–5266, doi:10.1002/2014JD022962, 2015.
- Kadyrov, N., Maksyutov, S., Eguchi, N., Aoki, T., Nakazawa, T., Yokota, T., and Inoue, G.: Role of simulated GOSAT total column CO₂ observations in surface CO₂ flux uncertainty reduction, *J. Geophys. Res.-Atmos.*, 114, D21208, doi:10.1029/2008JD011597, 2009.
- Koch, G. J., Beyon, J. Y., Gibert, F., Barnes, B. W., Ismail, S., Petros, M., Petzar, P. J., Yu, J., Modlin, E. A., Davis, K. J., and Singh, U. N.: Side-line tunable laser transmitter for differential absorption lidar measurements of CO₂: design and application to atmospheric measurements, *Appl. Opt.*, 47, 944–956, doi:10.1364/AO.47.000944, 2008.
- Koide, M., Taguchi, M., Fukunishi, H., and Okano, S.: Ground-based remote sensing of methane height profiles with a tunable diode laser heterodyne spectrometer, *Geophys. Res. Lett.*, 22, 401–404, doi:10.1029/95GL00051, 1995.
- Kostiuk, T.: Physics and chemistry of upper atmospheres of planets from infrared observations, *Infrared Phys. Technol.*, 35, 243–266, doi:10.1016/1350-4495(94)90084-1, 1994.
- Kostiuk, T. and Mumma, M. J.: Remote sensing by IR heterodyne spectroscopy, *Appl. Opt.*, 22, 2644–2654, doi:10.1364/AO.22.002644, 1983.
- Kostiuk, T., Mumma, M. J., Hillman, J. J., Buhl, D., Brown, L. W., Faris, J. L., and Spears, D. L.: NH₃ spectral line measurements on Earth and Jupiter using a 10 μ m superheterodyne receiver, *Infrared Phys.*, 17, 431–439, doi:10.1016/0020-0891(77)90049-5, 1977.
- Kostiuk, T., Fast, K. E., Livengood, T. A., Hewagama, T., Goldstein, J. J., Espenak, F., and Buhl, D.: Direct measurement of winds on Titan, *Geophys. Res. Lett.*, 28, 2361–2364, doi:10.1029/2000GL012617, 2001.
- Le Quééré, C., Raupach, M. R., Canadell, J. G., Marland, G., Bopp, L., Ciais, P., Conway, T. J., Doney, S. C., Feely, R. A., Foster, P., Friedlingstein, P., Gurney, K., Houghton, R. A., House, J. I., Huntingford, C., Levy, P. E., Lomas, M. R., Majkut, J., Metzl, N., Ometto, J. P., Peters, G. P., Prentice, I. C., Randerson, J. T., Running, S. W., Sarmiento, J. L., Schuster, U., Sitch, S., Takahashi, T., Viogy, N., van der Werf, G. R., and Woodward, F. I.: Trends in the sources and sinks of carbon dioxide, *Nat. Geosci.*, 2, 831–836, doi:10.1038/ngeo0689, 2009.
- Le Quééré, C., Andres, R. J., Boden, T., Conway, T., Houghton, R. A., House, J. I., Marland, G., Peters, G. P., van der Werf, G. R., Ahlström, A., Andrew, R. M., Bopp, L., Canadell, J. G., Ciais, P., Doney, S. C., Enright, C., Friedlingstein, P., Huntingford, C., Jain, A. K., Jourdain, C., Kato, E., Keeling, R. F., Klein Goldewijk, K., Levis, S., Levy, P., Lomas, M., Poulter, B., Raupach, M. R., Schwinger, J., Sitch, S., Stocker, B. D., Viogy, N., Zaehle, S., and Zeng, N.: The global carbon budget 1959–2011, *Earth Syst. Sci. Data*, 5, 165–185, doi:10.5194/essd-5-165-2013, 2013.
- Marquis, M. and Tans, P.: Carbon Crucible, *Science*, 320, 460–461, doi:10.1126/science.1156451, 2008.
- Melroy, H. R., Wilson, E. L., Clarke, G. B., Ott, L. E., Mao, J., Ramanathan, A. K., and McLinden, M. L.: Autonomous field measurements of CO₂ in the atmospheric column with the miniaturized laser heterodyne radiometer (Mini-LHR), *Appl. Phys. B*, 120, 609–615, doi:10.1007/s00340-015-6172-3, 2015.
- Menzies, R. T. and Seals, R. K.: Ozone Monitoring with an Infrared Heterodyne Radiometer, *Science*, 197, 1275–1277, doi:10.1126/science.197.4310.1275, 1977.

- Michalsky, J. J.: The Astronomical Almanac's algorithm for approximate solar position (1950–2050), *Sol. Energy*, 40, 227–235, doi:10.1016/0038-092X(88)90045-X, 1988.
- Miller, C. E., Crisp, D., DeCola, P. L., Olsen, S. C., Randerson, J. T., Michalak, A. M., Alkhaled, A., Rayner, P., Jacob, D. J., Suntharalingam, P., Jones, D. B. A., Denning, A. S., Nicholls, M. E., Doney, S. C., Pawson, S., Boesch, H., Connor, B. J., Fung, I. Y., O'Brien, D., Salawitch, R. J., Sander, S. P., Sen, B., Tans, P., Toon, G. C., Wennberg, P. O., Wofsy, S. C., Yung, Y. L., and Law, R. M.: Precision requirements for space-based data, *J. Geophys. Res.-Atmos.*, 112, D10314, doi:10.1029/2006JD007659, 2007.
- Myhre, G., Shindell, D., Bréon, F.-M., Collins, W., Fuglested, J., Huang, J., Koch, D., Lamarque, J.-F., Lee, D., Mendoza, B., Nakajima, T., Robock, A., Stephens, G., Takemura, T., and Zhang, H.: Anthropogenic and Natural Radiative Forcing, in: *Climate Change 2013: The Physical Science Basis. Contribution of Working Group I to the Fifth Assessment Report of the Intergovernmental Panel on Climate Change*, edited by: Stocker, T., Qin, D., Plattner, G.-K., Tignor, M., Allen, S. K., Boschung, J., Nauels, A., Xia, Y., Bex, V., and Midgley, P. M., Cambridge University Press, Cambridge, United Kingdom and New York, NY, USA, available at: <http://www.ipcc.ch/report/ar5/wg1/> (last access: 12 October 2015), 2013.
- Nisbet, E. and Weiss, R.: Top-Down Versus Bottom-Up, *Science*, 328, 1241–1243, doi:10.1126/science.1189936, 2010.
- O'Dell, C. W., Connor, B., Bösch, H., O'Brien, D., Frankenberg, C., Castano, R., Christi, M., Eldering, D., Fisher, B., Gunson, M., McDuffie, J., Miller, C. E., Natraj, V., Oyafuso, F., Polonsky, I., Smyth, M., Taylor, T., Toon, G. C., Wennberg, P. O., and Wunch, D.: The ACOS CO₂ retrieval algorithm – Part 1: Description and validation against synthetic observations, *Atmos. Meas. Tech.*, 5, 99–121, doi:10.5194/amt-5-99-2012, 2012.
- Parvitte, B., Zéninari, V., Thiébeaux, C., Delahaigne, A., and Courtois, D.: Infrared laser heterodyne systems, *Spectrochim. Acta A.*, 60, 1193–1213, doi:10.1016/j.saa.2003.07.006, 2004.
- Peylin, P., Law, R. M., Gurney, K. R., Chevallier, F., Jacobson, A. R., Maki, T., Niwa, Y., Patra, P. K., Peters, W., Rayner, P. J., Rödenbeck, C., van der Laan-Luijkx, I. T., and Zhang, X.: Global atmospheric carbon budget: results from an ensemble of atmospheric CO₂ inversions, *Biogeosciences*, 10, 6699–6720, doi:10.5194/bg-10-6699-2013, 2013.
- Ramanathan, A. K., Mao, J., Abshire, J. B., and Allan, G. R.: Remote sensing measurements of the CO₂ mixing ratio in the planetary boundary layer using cloud slicing with airborne lidar, *Geophys. Res. Lett.*, 42, 2055–2062, doi:10.1002/2014GL062749, 2015.
- Rayner, P. J. and O'Brien, D. M.: The utility of remotely sensed CO₂ concentration data in surface source inversions, *Geophys. Res. Lett.*, 28, 175–178, doi:10.1029/2000GL011912, 2001.
- Reda, I. and Andreas, A.: Solar position algorithm for solar radiation applications, *Sol. Energy*, 76, 577–589, doi:10.1016/j.solener.2003.12.003, 2004.
- Rodgers, C. D.: *Inverse Methods for Atmospheric Sounding: Theory and Practice*, World Scientific, ISBN-13: 978-981-02-2740-1, 2000.
- Rose, R. A. and Weidmann, D.: Remote sounding performances of a thermal IR LHR for monitoring atmospheric trace gases, CEOI Mission Study, STFC Rutherford Appleton Laboratory, Didcot, UK, 2013.
- Rothman, L. S., Gordon, I. E., Babikov, Y., Barbe, A., Chris Benner, D., Bernath, P. F., Birk, M., Bizzocchi, L., Boudon, V., Brown, L. R., Campargue, A., Chance, K., Cohen, E. A., Coudert, L. H., Devi, V. M., Drouin, B. J., Fayt, A., Flaud, J.-M., Gamache, R. R., Harrison, J. J., Hartmann, J.-M., Hill, C., Hodges, J. T., Jacquemart, D., Jolly, A., Lamouroux, J., Le Roy, R. J., Li, G., Long, D. A., Lyulin, O. M., Mackie, C. J., Massie, S. T., Mikhailenko, S., Müller, H. S. P., Naumenko, O. V., Nikitin, A. V., Orphal, J., Perevalov, V., Perrin, A., Polovtseva, E. R., Richard, C., Smith, M. A. H., Starikova, E., Sung, K., Tashkun, S., Tennyson, J., Toon, G. C., Tyuterev, V. G., and Wagner, G.: The HITRAN2012 molecular spectroscopic database, *J. Quant. Spectrosc. Ra.*, 130, 4–50, doi:10.1016/j.jqsrt.2013.07.002, 2013.
- Saito, R., Houweling, S., Patra, P. K., Belikov, D., Lokupitiya, R., Niwa, Y., Chevallier, F., Saeki, T., and Maksyutov, S.: TransCom satellite intercomparison experiment: Construction of a bias corrected atmospheric CO₂ climatology, *J. Geophys. Res.-Atmos.*, 116, D21120, doi:10.1029/2011JD016033, 2011.
- Schimmel, D., Stephens, B. B., and Fisher, J. B.: Effect of increasing CO₂ on the terrestrial carbon cycle, *P. Natl. Acad. Sci. USA*, 112, 436–441, doi:10.1073/pnas.1407302112, 2015.
- Sonnabend, G., Sornig, M., Krötz, P. J., Schieder, R. T., and Fast, K. E.: High spatial resolution mapping of Mars mesospheric zonal winds by infrared heterodyne spectroscopy of CO₂, *Geophys. Res. Lett.*, 33, L18201, doi:10.1029/2006GL026900, 2006.
- Sonnabend, G., Sornig, M., Krötz, P., Stupar, D., and Schieder, R.: Ultra high spectral resolution observations of planetary atmospheres using the Cologne tuneable heterodyne infrared spectrometer, *J. Quant. Spectrosc. Ra.*, 109, 1016–1029, doi:10.1016/j.jqsrt.2007.12.003, 2008.
- Stephens, B. B., Gurney, K. R., Tans, P. P., Sweeney, C., Peters, W., Bruhwiler, L., Ciais, P., Ramonet, M., Bousquet, P., Nakazawa, T., Aoki, S., Machida, T., Inoue, G., Vinnichenko, N., Lloyd, J., Jordan, A., Heimann, M., Shibistova, O., Langenfelds, R. L., Steele, L. P., Francey, R. J., and Denning, A. S.: Weak Northern and Strong Tropical Land Carbon Uptake from Vertical Profiles of Atmospheric CO₂, *Science*, 316, 1732–1735, doi:10.1126/science.1137004, 2007.
- Teich, M. C., Keyes, R. J., and Kingston, R. H.: Optimum heterodyne detection at 10.6 μm in photoconductive Ge:Cu, *Appl. Phys. Lett.*, 9, 357–360, doi:10.1063/1.1754611, 1966.
- Thompson, D. R., Chris Benner, D., Brown, L. R., Crisp, D., Malathy Devi, V., Jiang, Y., Natraj, V., Oyafuso, F., Sung, K., Wunch, D., Castaño, R., and Miller, C. E.: Atmospheric validation of high accuracy CO₂ absorption coefficients for the OCO-2 mission, *J. Quant. Spectrosc. Ra.*, 113, 2265–2276, doi:10.1016/j.jqsrt.2012.05.021, 2012.
- Tsai, T. R., Rose, R. A., Weidmann, D., and Wsocki, G.: Atmospheric vertical profiles of O₃, N₂O, CH₄, CCl₂F₂, and H₂O retrieved from external-cavity quantum-cascade laser heterodyne radiometer measurements, *Appl. Opt.*, 51, 8779–8792, doi:10.1364/AO.51.008779, 2012.
- Weidmann, D., Reburn, W. J., and Smith, K. M.: Ground-based prototype quantum cascade laser heterodyne radiometer for atmospheric studies, *Rev. Sci. Instrum.*, 78, 73107, doi:10.1063/1.2753141, 2007a.
- Weidmann, D., Reburn, W. J., and Smith, K. M.: Retrieval of atmospheric ozone profiles from an infrared quantum cascade

- laser heterodyne radiometer: results and analysis, *Appl. Opt.*, 46, 7162–7171, doi:10.1364/AO.46.007162, 2007b.
- Weidmann, D., Tsai, T., Macleod, N. A., and Wysocki, G.: Atmospheric observations of multiple molecular species using ultra-high-resolution external cavity quantum cascade laser heterodyne radiometry, *Opt. Lett.*, 36, 1951–1953, doi:10.1364/OL.36.001951, 2011a.
- Weidmann, D., Perrett, B. J., Macleod, N. A., and Jenkins, R. M.: Hollow waveguide photomixing for quantum cascade laser heterodyne spectro-radiometry, *Opt. Express*, 19, 9074–9085, doi:10.1364/OE.19.009074, 2011b.
- Wilson, E. L., McLinden, M. L., Miller, J. H., Allan, G. R., Ott, L. E., Melroy, H. R., and Clarke, G. B.: Miniaturized laser heterodyne radiometer for measurements of CO₂ in the atmospheric column, *Appl. Phys. B*, 114, 385–393, doi:10.1007/s00340-013-5531-1, 2014.
- Wirtz, D., Sonnabend, G., and Schieder, R. T.: THIS: a tuneable heterodyne infrared spectrometer, *Spectrochim. Acta A.*, 58, 2457–2463, doi:10.1016/S1386-1425(02)00062-8, 2002.
- WMO/GAW: 17th WMO/IAEA Meeting on Carbon Dioxide, Other Greenhouse Gases and Related Tracers Measurement Techniques (GGMT-2013), Beijing, China, 10–13 June 2013, available at: <http://www.wmo.int/pages/prog/arep/gaw/gaw-reports.html> (last access: 13 October 2015), 2014.
- Wunch, D., Toon, G. C., Blavier, J.-F. L., Washenfelder, R. A., Notholt, J., Connor, B. J., Griffith, D. W. T., Sherlock, V., and Wennberg, P. O.: The Total Carbon Column Observing Network, *Philos. Trans. R. Soc. Lond. Math. Phys. Eng. Sci.*, 369, 2087–2112, doi:10.1098/rsta.2010.0240, 2011.
- Yang, Z., Washenfelder, R. A., Keppel-Aleks, G., Krakauer, N. Y., Randerson, J. T., Tans, P. P., Sweeney, C., and Wennberg, P. O.: New constraints on Northern Hemisphere growing season net flux, *Geophys. Res. Lett.*, 34, L12807, doi:10.1029/2007GL029742, 2007.